Chapter 13
Mapping the Distribution of Fluids in the Crust and Lithospheric Mantle Utilizing Geophysical Methods

Martyn Unsworth and Stéphane Rondenay

Abstract Geophysical imaging provides a unique perspective on metasomatism, because it allows the present day fluid distribution in the Earth's crust and upper mantle to be mapped. This is in contrast to geological studies that investigate mid-crustal rocks have been exhumed and fluids associated with metasomatism are absent. The primary geophysical methods that can be used are (a) electromagnetic methods that image electrical resistivity and (b) seismic methods that can measure the seismic velocity and related quantities such as Poisson's ratio and seismic anisotropy. For studies of depths in excess of a few kilometres, the most effective electromagnetic method is magnetotellurics (MT) which uses natural electromagnetic signals as an energy source. The electrical resistivity of crustal rocks is sensitive to the quantity, salinity and degree of interconnection of aqueous fluids. Partial melt and hydrogen diffusion can also cause low electrical resistivity. The effects of fluid and/or water on seismic observables are assessed by rock and mineral physics studies. These studies show that the presence of water generally reduces the seismic velocities of rocks and minerals. The water can be present as a fluid, in hydrous minerals, or as hydrogen point defects in nominally anhydrous minerals. Water can further modify seismic properties such as the Poisson's ratio, the quality factor, and anisotropy. A variety of seismic analysis methods are employed to measure these effects in situ in the crust and lithospheric mantle and include seismic tomography, seismic reflection, passive-source converted and scattered wave imaging, and shear-wave splitting analysis. A combination of magnetotelluric and seismic data has proven an effective tool to study the fluid

---

M. Unsworth (✉)
University of Alberta, Edmonton, AB T6G 2J1, Canada
e-mail: unsworth@UAlberta.ca

S. Rondenay
University of Bergen, Bergen 5020, Norway

Massachusetts Institute of Technology, Cambridge, MA 02139, USA
e-mail: rondenay@geo.uib.no

D.E. Harlov and H. Austrheim, *Metasomatism and the Chemical Transformation of Rock*, Lecture Notes in Earth System Sciences,
DOI 10.1007/978-3-642-28394-9_13,

distribution in zones of active tectonics such as the Cascadia subduction zone. In this location fluids can be detected as they diffuse upwards from the subducting slab and hydrate the mantle wedge. In a continent-continent collision, such as the Tibetan Plateau, a pervasive zone of partial melting and aqueous fluids was detected at mid-crustal depths over a significant part of the Tibetan Plateau. These geophysical methods have also been used to study past metasomatism ancient plate boundaries preserved in Archean and Proterozoic aged lithosphere.

13.1 Introduction

Metasomatism occurs in the crust and upper mantle and causes a profound change in the composition of rocks. The presence of even small amounts of aqueous or magmatic fluids often controls the rate of metamorphic reactions. Most of our knowledge of metamorphic and metasomatic processes is based on geochemical studies of these rocks when they have been exhumed and exposed at the surface. This means that the process of metasomatism is being studied in ancient orogens, when the fluids are no longer present, except in isolated fluid inclusions. Being able to observe the fluids that cause metasomatism in real time is essential to understanding how this process occurs. Geophysics allows us to map in situ fluid distributions in real time, because the presence of fluids can significantly change the physical properties of a rock, primarily electrical resistivity and seismic velocity. Subsurface variations in these properties can be measured with surface based geophysical data. Electromagnetic methods can image electrical resistivity and seismic methods can image seismic velocities and related quantities such as Poisson's ratio.

In this chapter the physical basis for using geophysical observations to map the present day fluid distribution in the crust and upper mantle is described. This includes (1) an understanding of how the presence of fluids changes the properties of the rock, (2) how to measure these properties from the surface with geophysical imaging, and (3) a number of case studies that illustrate how geophysical data can determine the fluid distribution in locations where metasomatism is occurring. Metasomatism changes the mineralogy of crustal and upper mantle rocks in a permanent way, which can provide evidence of past metasomatism. Examples of this type of observation are also discussed.

13.2 Electromagnetic Methods

13.2.1 Electrical Resistivity of Rocks

The electrical resistivity, or reciprocal conductivity, of a rock contains information about its composition and structure. To understand the resistivity of crustal and upper mantle rocks, it is first necessary to consider the resistivity of the minerals that make up these rocks.

The electrical resistivity of a pure mineral depends on two factors: (1) the density of charge carriers, typically electrons or ions and (2) the ease with which these charge carriers can move through the mineral (mobility). An extreme example is Cu, which has a very high density of charge carriers (electrons) that are weakly attached to atoms in the lattice and move very easily, resulting in a very low electrical resistivity ($\rho = 10^{-10}$ Ωm). In contrast, in diamond the C atoms are rigidly attached to the crystal lattice and cannot easily move through the crystal to carry electric current. This makes the electrical resistivity of diamond very high, typically more than 10^{10} Ωm.

Pure materials are only found locally in the Earth, with most rocks consisting of a complex mixture of materials. Thus to calculate the overall resistivity of a rock, the resistivity of the constituents must be considered, along with their geometric distribution. A common situation in the crust and upper mantle is for the rock to be characterized by two phases. The bulk of the rock comprises mineral grains that have a very high resistivity, while the pore space is occupied by a second phase that has a low resistivity. Even if the second phase is volumetrically small, it can significantly influence the overall resistivity of the rock. This is a common occurrence with, for example, saline aqueous fluids or melt occupying the space between the grains. Other conducting phases can be present and include sulphides or graphite. Note that this is in contrast to seismic velocity where contrasts in velocities are smaller.

The focus of this chapter is on the detection of metasomatizing fluids, so the emphasis will be on crustal rocks containing saline fluids and partial melts. In this case the overall resistivity of the rock is dominated by (a) the resistivity of the fluid, (b) the amount of fluid, and (c) the geometric distribution of the fluid. These factors are reviewed below.

13.2.1.1 Resistivity of Aqueous Fluids

First, the electrical resistivity of saline fluids as a function of composition, pressure and temperature, is reviewed. As the salinity increases the number of charge carriers (anions and cations) increases and the resistivity decreases. A number of empirical equations have been developed to characterize this behaviour (Block 2001; Meju 2000). At low salinities the increase in conductivity with salinity is nearly linear.

To interpret crustal resistivity values observed at mid and lower crustal depths, it is important to consider effects of temperature on the resistivity of aqueous fluids. Temperature effects are summarized in Figs. 13.1 and 13.2, based on the studies of Ussher et al. (2000) and Nesbitt (1993). The results of Ussher et al. (2000) are based on the original data of Ucok et al. (1980). At all temperatures, increasing salinity produces a monotonic decrease in resistivity as more charge carriers become

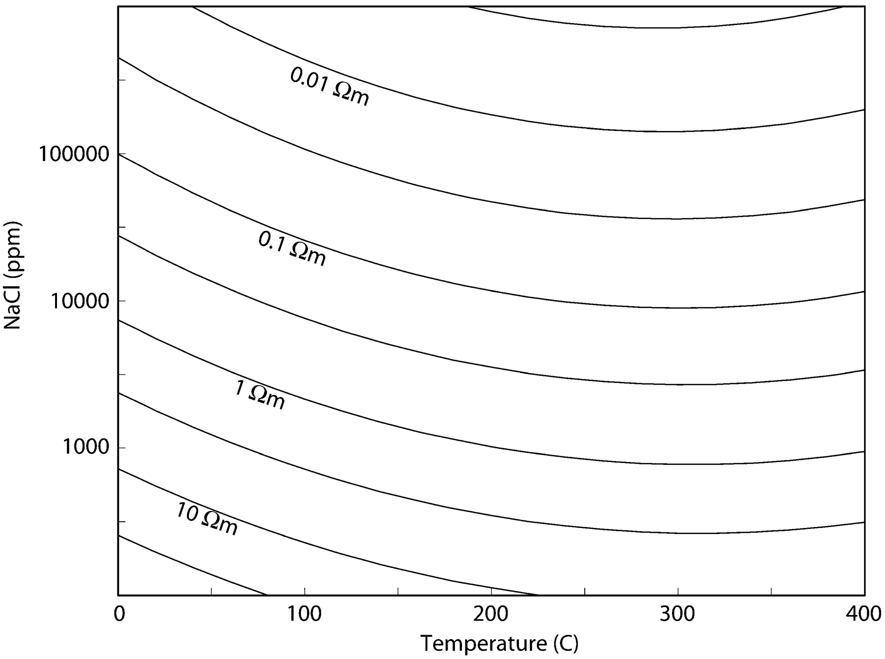

Fig. 13.1 Contour plot of electrical resistivity as a function of salinity and temperature for saline crustal fluids (Adapted from Ussher et al. (2000))

available. At constant salinity, increasing temperatures (0–300°C) causes a decrease in resistivity as fluid viscosity decreases and the ions are able to move more easily through the solution. Above 300°C an increase in resistivity is observed and this effect is correlated with decreasing solution density. The decreased density causes an increase in ion pairing that reduces the density of available charge carriers (Nesbitt 1993).

Pressure also influences the electrical resistivity of the aqueous fluid. A detailed summary of the pressure temperature dependence of resistivity is described by Quist and Marshall (1968) and number of similar studies. Nesbitt (1993) summarizes information about aqueous fluid resistivity, with specific application to conditions found in the Earth's crust. Figure 13.2 illustrates the combined effects of temperature and pressure on a KCl solution of varying concentrations based on the data of Nesbitt (1993). Below 300°C, the resistivity decreases with increasing temperature and pressure has very little effect. The lowest resistivity occurs around 300°C. At temperatures above 300°C pressure has a significant influence on resistivity because of the resistivity density correlation described above. Note that in this range, increasing pressure decreases the resistivity by increasing the solution density.

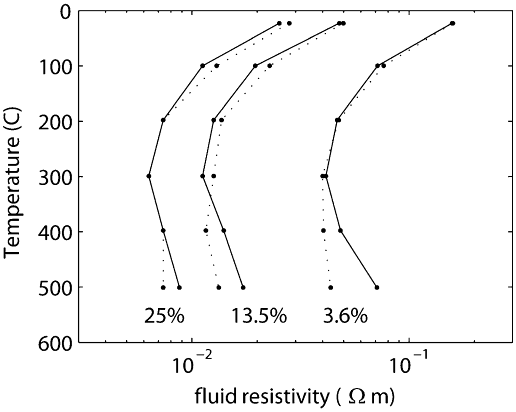

Fig. 13.2 Effect of temperature and pressure on the resistivity of a KCl solution (Adapted from Fig. 1 in Nesbitt (1993)). For each salinity value, two pressures are shown (*continuous curve* = 1Kbar; *dashed curve* = 3Kbar). Percentage values indicate salinity.

In interpreting crustal resistivity values measured with magnetotelluric data, it is important to understand depth variations in fluid resistivity due to simultaneous increases in both pressure and temperature. Figure 13.3a shows this effect for a geothermal gradient of 30°C per km and a lithostatic pressure gradient (25 MPa per km or 0.25 kb per km).

Salts are not the only source of dissolved ions in crustal aqueous fluids. Carbon is widely observed in the Earth's crust in a variety of forms, including diamond, graphite, hydrocarbons, and carbon dioxide. Carbon dioxide will dissolve in water to form H^+ and HCO_3^- ions that will act as charge carriers and lower the electrical resistivity of the fluid. Nesbitt (1993) summarizes data that show that an increase in CO_2 concentration will lower the resistivity of the solution (Fig. 13.3b). Note that the electrical resistivity of these solutions exhibits a greater temperature dependence than salt solutions. As with salt solutions, increasing temperature causes a decrease in resistivity up to a temperature of 300°C, after which the resistivity increases.

Of course, many aqueous solutions contain both dissolved salts and carbon dioxide. The synthesis of Nesbitt (1993) suggests that at upper crustal levels, the salt will dominate the fluid resistivity, while in the mid-crust the dissolved CO_2 will dominate the fluid resistivity under lithostatic conditions.

In summary, it can be seen that aqueous fluids will have resistivities in the range 0.01–10 Ωm. Knowledge of the fluid composition, either from well measurements or fluid inclusions, plus thermal and pressure gradients, are also needed to give a more precise estimate of the fluid resistivity.

13.2.1.2 Electrical Resistivity of Partial Melts

Under certain conditions, the presence of aqueous fluids can cause partial melting. As the partial melts migrate, they can cause metasomatism in both the crust and

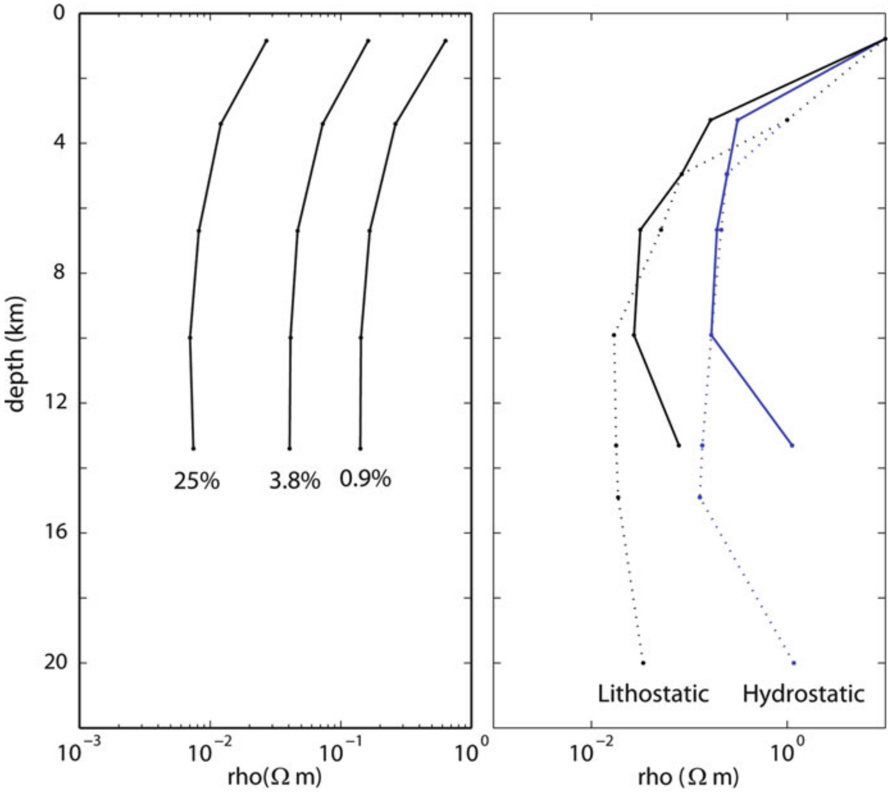

Fig. 13.3 Variation of resistivity as a function of depth for an aqueous fluid containing (**a**) KCl and (**b**) $KHCO_3$ solution assuming geothermal gradients of 20°C/km (*solid curve*) and 30°C/km (*dashed curve*) (Based on data from Nesbitt (1993)). Percentage values indicate salinity.

upper mantle (Prouteau et al. 2001). Partial melt has a low resistivity, since the ions can move relatively easily through the liquid. The resistivity of the melt depends on the amount of dissolved water and the petrology, and is generally in the range 1–0.1 Ωm (Wannamaker 1986; Li et al. 2003).

13.2.1.3 Resistivity of Whole Rock for Various Pore Fluid Distributions

As described above, in a typical rock, the low resistivity phase dominates the bulk resistivity of the sample, even if the minor phase occupies a very small fraction of the whole rock. The second factor that controls the overall resistivity is the geometric distribution of a low resistivity minor phase, such as a free fluid

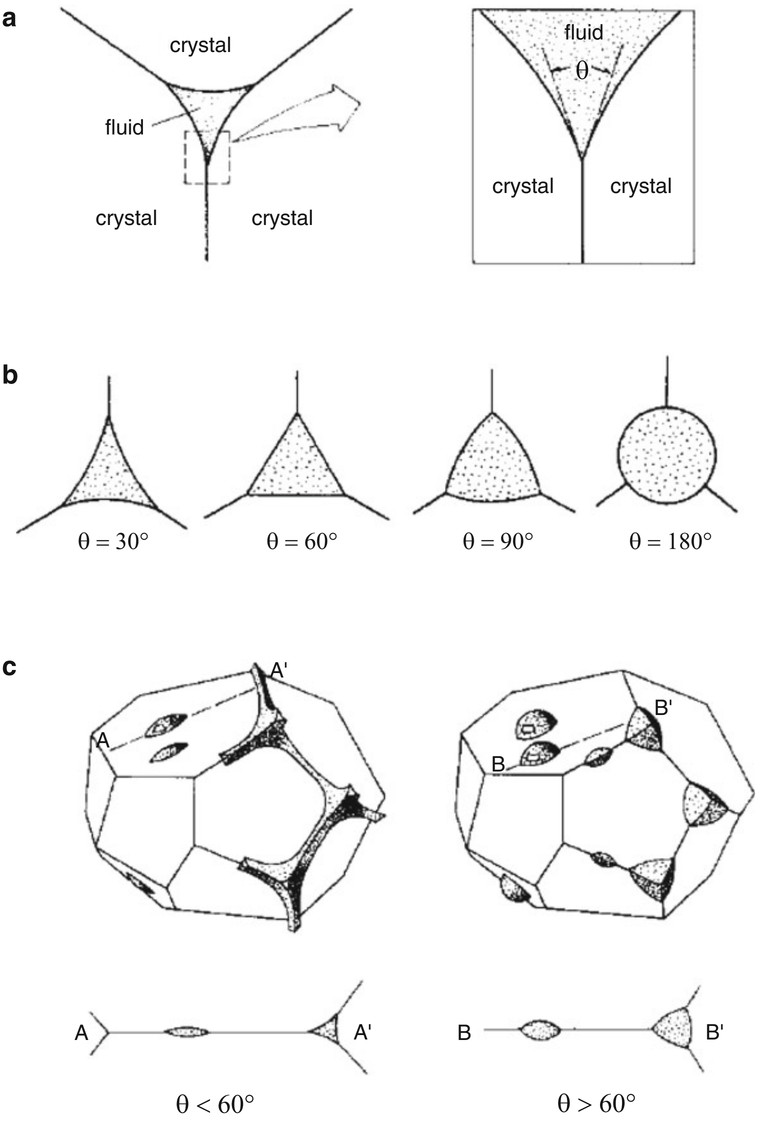

Fig. 13.4 Illustration of the effect of the dihedral angle (θ) on the fluid distribution in a porous rock (Adapted from Watson and Brenan 1987). For $\theta > 60°$ the fluid will be distributed as isolated inclusions, while for $\theta < 60°$ it will be distributed in tubes along the grain boundaries

phase. This effect is illustrated in Fig. 13.4. If the fluid is located in isolated pores, it will not form an interconnected network that can effectively conduct electricity. In contrast, if the fluid is distributed in tubes along the grain boundaries then a continuous network exists that will conduct electric current.

Thus it is important to be able to predict the distribution of a fluid in a host rock. This depends on the relative surface energy of the fluid and the mineral crystals, and can be visualized through the dihedral or wetting angle as shown in Fig. 13.4. Laboratory data for aqueous fluids and partial melts are reviewed in the following sections.

It can be shown that, with a low dihedral angle, the pore fluid will effectively wet all grain boundaries, while at high values, the fluid will be located in isolated inclusions. At low fluid fractions (<1%), a dihedral angle $\theta = 60°$ represents the boundary between these fluid distributions. At higher fluid fractions this angle may increase slightly (Watson and Brenan 1987). The dihedral angle is very important as it controls many of the properties of the rock. A low dihedral angle produces interconnection that will result in a low resistivity. It will also allow fluids to migrate rapidly through the rock matrix, which is very significant in the context of metasomatism. Interconnection of the fluids will also reduce the strength of the rock.

Dihedral Angles of Aqueous Fluids in Crustal and Upper Mantle Rocks

Watson and Brenan (1987) studied the dihedral angles of H_2O–CO_2 fluids in synthetic rock samples at temperatures of 950–1,150°C and pressures of 1 GPa = 10 Kbar, corresponding to lower crustal conditions. The study showed that under these conditions, the dihedral angle for pure water in a quartz matrix was 57° and 65° for pure water in an olivine matrix. The addition of CO_2 caused a marked increase to values around 90° in both lithologies. Thus crustal fluids containing significant amounts of CO_2 are unlikely to be interconnected at mid and lower crustal conditions. In contrast, the addition of solutes caused a reduction in dihedral angle below 60° indicating that saline fluids could form an interconnected network along the grain edges. Additional studies of dihedral angles in crustal fluids are presented by Brenan and Watson (1988).

The study of dihedral angles in fluid saturated crustal rocks was extended by Holness (1992) and (1993) to consider a range of pressures and temperatures. Holness (1992) showed that at 800°C there was a strong pressure control on the dihedral angle. Holness (1993) confirmed that dihedral angles greater than 60° were present over a broad range of pressure and temperature conditions as shown in Fig. 13.5. This study also confirmed that the presence of CO_2 raises the dihedral angle, while dissolved salts can dramatically lower the dihedral angle. It should also be noted that when multiple fluids are present, they can become immiscible (Gibert et al. 1998).

In summary, it appears that fluids can be interconnected in two distinct pressure-temperature windows. The first occurs at temperatures close to the melting point, and the second at the lower temperatures found in regions with a geothermal gradient typical of a craton.

Fig. 13.5 (**a**) Plot of dihedral angle as a function of temperature and pressure (Taken from Fig. 6 in Holness 1993). Lower dihedral angles are expected if the water has a high salinity. (**b**) Metamorphic facies. *Blue line* denotes a cratonic geothermal gradient. *PP* Prehenite-pumpellyite, *EA* Epidote-amphibolite, *Z* zeolite

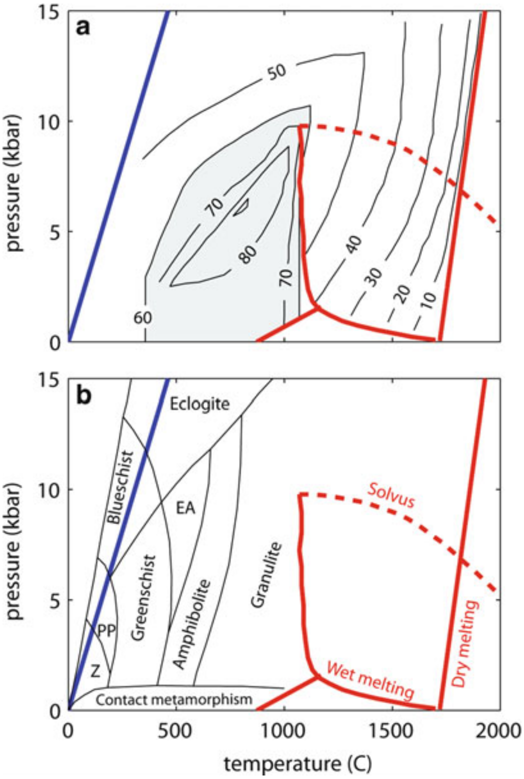

Dihedral Angles of Partial Melts in Crustal and Upper Mantle Rocks

A number of laboratory studies have investigated the dihedral angles found in partial melts. ten Grotenhuis et al. (2005) studied basaltic melts and showed that effective interconnection occurred, implying a dihedral angle below 60°. Holness (2006) studied the melt-solid dihedral angles in field samples and reported the following values: plagioclase (25°), clinopyroxene (38°), olivine (29°), quartz (18°), and leucite (20°). Mamaus et al. (2004) studied partial melts with a more felsic (SiO_2-rich) composition and showed a median value for dihedral angles of 50°. This study also showed that anisotropy of the olivine required a melt fraction of 0.3% for interconnection to occur. Their study raised questions about the ability of silica-rich melts to act as metasomatizing fluids. This is because the melt was unable to infiltrate a rock at low melt fraction.

It should be noted that fluid distributions measured in the laboratory may not be representative of those found in regions undergoing active deformation. Shear will redistribute the fluid and can often generate a higher degree of interconnection than found in undeformed samples. Laboratory studies of this effect include both rocks containing aqueous fluids (Tullis et al. 1996) and partial melts (Hasalová et al. 2008; Schulmann et al. 2008).

13.2.1.4 Bulk Resistivity of Rocks Containing Fluids

Having considered the typical situation of a high conductivity fluid permeating a matrix of low conductivity grains, we can now consider the bulk resistivity of the rock. This analysis will consider both aqueous fluids and the partial melts. The type of fluid present depends on temperature and composition of the rocks. In dry rocks, a temperature of 1,100°C may be needed to initiate melting, and the fluids will be partial melts. If the rocks are water saturated then melting will begin at lower temperatures and a range of fluids can be expected with aqueous fluids trending into partial melts.

A number of empirical relationships have been developed to predict the bulk resistivity of a fluid bearing rock. These equations use the terms described in previous sections. The bulk resistivity is primarily dependent on the fluid resistivity and the fluid geometry (degree of interconnection).

Archie's Law is an empirical relationship that was originally developed for the interpretation of resistivity logs measured in water saturated sedimentary rocks (Archie 1942). It was developed to allow resistivity measured by well logging to be used to infer the type of fluid present in the surrounding rock layers. The physical basis was the fact that hydrocarbons have a much higher resistivity than water. Archie's Law states that the bulk resistivity ρ of a fluid saturated rock can be written as

$$\rho = C\rho_w \Phi^{-m}$$

where ρ_w is the resistivity of the fluid, Φ is the porosity, and m is a constant, termed the cementation factor, that depends on the fluid distribution (interconnectivity of the pores). Values of m in the range 1–1.3 correspond to a fluid that is well connected, equivalent to a dihedral angle $\theta < 60°$. Values of $m = 2$, or greater, correspond to a fluid located in isolated pores, with $\theta > 60°$. C is an empirical constant, typically close to 1. It should be noted that the resistivity of the rock matrix does not appear in the equation, since it is assumed that the fluid is much more conductive than the mineral grains and all electrical conduction occurs through the pore fluid. Archie's Law also assumes that no clay minerals are present in the rock, as these would provide an alternate pathway for electric current flow and invalidate Archie's Law as a way of converting bulk resistivity into an estimate of porosity (Worthington 1993). A more general form of Archie's Law considers the case of partial saturation, and it has also been adapted to model three phase systems (Glover et al. 2000).

Archies Law was developed for the analysis of sedimentary rocks containing aqueous pore fluids. It has been successfully applied to rocks where the fluid is a partial melt. Owing to the difficulties of working with molten rocks, very few experimental studies of the resistivity of partial melts have been reported. Roberts and Tyburczy (1999) investigated a mixture of olivine and MORB, with the melt fraction being controlled by the temperature. This study showed that Archie's Law could be used to understand the bulk resistivity of partial melts with $C = 0.73$ and $m = 0.98$, implying a good interconnection of the grain boundary melt. The approach of Roberts and Tyburczy (1999) has the complication that the melt composition varied with temperature, and only a limited range of melt fractions

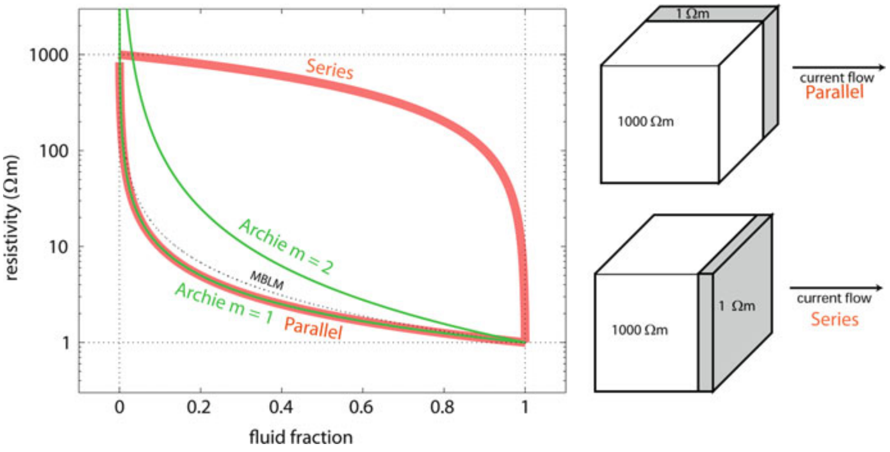

Fig. 13.6 Plot of bulk resistivity as a function of porosity for a rock containing a pore fluid with resistivity 1 Ωm and with mineral grains with a resistivity 1,000 Ωm. Series and parallel curves show maximum and minimum resistivities possible for a given fluid content. Fluid is shown in *grey* in panels on the *right*. *Green curves* show values for Archie's Law with m = 1 and 2. Note that m = 1 is essentially the same as the parallel circuit with the best possible interconnection. Also note that Archie's Law is incorrect at low fluid fractions when conduction through the mineral grains becomes significant

could be considered. A novel approach to this problem was presented by ten Grotenhuis et al. (2005) who studied the melt geometry in a synthetic olivine sample at atmospheric pressure, with the melt fraction controlled by the addition of glass. Analysis of quenched samples showed that effective interconnection occurs at melt fractions in the range 1–10%. The resistivity of the samples was well described by Archies Law with constant C = 1.47 and cementation factor m = 1.3, which represents a lower degree of interconnection than in the study of Roberts and Tyburczy (1999). The discovery of the crustal low resistivity zone beneath Southern Tibet has motivated new studies of the physical properties of partial melts. Laboratory studies by Gaillard (2004) showed that the resistivity of hydrous granitic melts at the appropriate pressures and temperatures were in "perfect agreement with those inferred from MT data" beneath Southern Tibet.

Other empirical equations and models have been developed to model the bulk resistivity of a rock consisting of a conductive fluid and a resistive matrix. The modified block layer model (MBLM) model was developed by Partzsch et al. (2000) and assumes effective interconnection of the pore fluid. This model explicitly considers conduction through the mineral grains. This becomes important at higher temperatures since it causes the ion mobility in the rock matrix to increase and contribute to the overall resistivity of the rock. The bulk resistivities predicted by MBLM and Archie's Law are illustrated in Fig. 13.6. Also shown are the maximum and minimum possible resistivities, assuming that the fluid is distributed in sheets parallel (ρ_{par}) and perpendicular (ρ_{perp}) to the electric current flow. Note that ρ_{par} (Φ) and Archie's Law, with a cementation factor m = 1, give virtually identical curves, since both assume effective interconnection of the low resistivity fluid phase. These results are similar to those for the MBLM.

Figure 13.6 also shows that Archie's Law, with $m = 2$, predicts a higher resistivity at a given value of Φ than with $m = 1$. This is because interconnection is less effective with m = 2 and more fluid is needed to produce the same network at $m = 2$. This figure also shows the limitations of Archie's Law, since the $m = 2$ curve predicts a resistivity greater than the rock matrix at low values of Φ, which is clearly non-physical. In these models, the conducting phase can be aqueous fluids or partial melts. The models can be applied to rocks containing a small amount of a low resistivity phase such as graphite or disseminated sulphide minerals.

Some authors have suggested that surface conduction mechanisms occurring along grain boundaries may control the bulk resistivity of crustal and upper mantle rocks (ten Grotenhuis et al. 2004). In this scenario, low resistivity anomalies could be due to regions with smaller grain size, and not an enhanced fluid content as suggested above.

13.2.1.5 Electrical Anisotropy

A range of field and laboratory studies suggest that both crustal and upper mantle rocks can exhibit electrical anisotropy (Wannamaker 2005). In the case of crustal rocks, this occurs when the rock contains a low resistivity phase that is distributed anisotropically in the rock. For example, graphite is commonly found in fractures in rocks that have undergone extensive deformation. This produces electrical anisotropy that has been measured both with borehole logging (Eisel and Haak 1999) and with magnetotelluric surveys (Kellett et al. 1992; Heise and Pous 2003). A similar effect can occur when crustal rocks contain fluids that are present in fractures that are not uniformly distributed.

There is significant evidence that the upper mantle can be electrically anisotropic and different mechanisms have been proposed as an explanation (Gatzemeier and Moorkamp 2004).

(a) One explanation proposes that in the upper mantle, free water can dissociate into ions which act as charge carriers to transport electric current. The diffusion of H ions, along grain boundaries, has been proposed as an explanation for spatial variations in upper mantle conductivity (Karato 1990). Since olivine grains are preferentially oriented by shearing during upper mantle flow, this may cause electrical anisotropy (Simpson 2001; Simpson and Tommasi 2005).

(b) Another explanation, for upper mantle anisotropy, suggested that in the roots of the Archean Superior Craton, was caused by graphite deposited by metasomatism (Kellett et al. 1992; Mareschal et al. 1995).

(c) Finally it has been proposed that anisotropic distribution of partial melt could cause electrical anisotropy in the upper mantle, specifically in the asthenosphere. However, the study of Gatzemeier and Moorkamp (2004) suggested that this could not explain the anisotropy observed beneath Germany.

It should be noted that magnetotelluric (MT) measurements cannot determine the length scale of the anisotropy if it is less than the skin depth of the MT signals. It can also be very difficult to distinguish between heterogeneous isotropic resistivity structures and anisotropic resistivity structures. This requires high quality MT datasets with a high spatial density of measurements. It has been shown that measurements of the vertical magnetic field are very useful in this respect (Brasse et al. 2009).

13.2.1.6 Non-Uniqueness in Interpreting Electrical Resistivity Measurements

Finally it should be stressed that there is an inherent non-uniqueness in interpreting the electrical resistivity of crustal and mantle rocks. The laboratory studies listed above, and empirical observations derived from them, can be considered a forward calculation, i.e. starting from a particular rock and fluid composition, the overall electrical resistivity of the rock can be predicted. In contrast, the inverse problem is much more complicated since an observed resistivity for a particular rock layer must be interpreted in terms of composition. This process is inherently non-unique at many levels as there are multiple causes for low resistivity (aqueous fluids, melt, H ion diffusion etc.). A clear example of this is the ongoing debate over the reason for the high conductivities observed in the lower crust. The available evidence has been taken to support both graphite or aqueous fluids as an explanation for the elevated conductivity (Yardley and Valley 1997; Wannamaker 2000). This is discussed in detail later in this chapter.

13.2.2 Measuring the Electrical Resistivity of the Earth at Depth

The results described in the previous section were based on laboratory measurements of the electrical resistivity of rocks. These studies are typically made on samples a few centimetres across.

Measuring the resistivity of in situ rocks is much more challenging, since indirect methods must be employed. These can be divided into (a) well-logging that measures resistivity of the rocks within a few metres of a borehole, and (b) geophysical studies that sample volumes up to depths of hundreds of kilometres with a horizontal extent of tens of kilometres. Resistivity log data can provide a valuable check on resistivity models derived from geophysical studies, and vice versa.

During well-logging, the resistivity of the subsurface rocks can be measured with a range of tools that use either galvanic or inductive coupling (Ellis and Singer 2008). Resistivity measurements, made by well-logging, have the advantage that the measurement is made with the tool relatively close to the rocks being studied. However, it does not provide measurements of a large volume away from the borehole and is inherently limited by the depth extent of the well.

Thus, measuring the resistivity of rocks under in situ conditions at depth in the crust or upper mantle requires the use of geophysical imaging, which is the focus of the following section.

For shallow investigations of subsurface electrical resistivity, methods using direct electrical current are very effective. These methods inject current into the ground with metal stakes and can give multi-dimensional images of near surface resistivity structure. However, they are inherently limited in their depth of penetration because the electrode spacing must be comparable to the depth of investigation. Sounding to depths in excess of 1 km becomes logistically complicated. In contrast, the depth of investigation with electromagnetic methods can be varied by simply changing the frequency of the signal. Systems, using a small transmitter, can image the crust to depth of a few kilometres, and some controlled source methods may reach mid-crustal depths (Strack et al. 1990). However, for deeper imaging, naturally occurring low frequency EM signals represent the ideal choice. This is the geophysical imaging technique called magnetotellurics (MT), which is the most suitable for studies of crustal and upper mantle resistivity (Simpson and Bahr 2005).

In magnetotelluric exploration, natural EM signals are used to probe the electrical resistivity of the subsurface. These waves are generated by global lightning activity (>1 Hz) and by magnetospheric variations caused by time-varying interactions between the solar wind and the geomagnetic field (<1 Hz). Figure 13.7 shows electromagnetic waves with two frequencies incident on the surface of the Earth. Most of the energy is reflected back into the atmosphere, but a small fraction enters the Earth and diffuses downwards. The depth to which the EM signal penetrates is controlled by the skin depth, which is defined in metres as:

$$\delta = 503\sqrt{\frac{\rho}{f}}$$

where the electromagnetic signal has a frequency f and the Earth has a uniform resistivity, ρ. This equation is illustrated in Fig. 13.8. Note that as the frequency is decreased, the depth of penetration (δ) increases. Thus a measurement of the depth variation in resistivity can be made by simply measuring natural electromagnetic signals over a range of frequencies. Similarly, it can be seen that the depth of penetration of signal, at a given frequency, will vary according to the subsurface resistivity. Low resistivity rocks can greatly limit the depth of investigation with MT.

When the incident, reflected, and transmitted waves are analysed, it can be shown that a simple equation can be derived for the resistivity of the Earth. Suppose the horizontal surface components of the electric and magnetic fields are E_x and H_y at a frequency f. The apparent resistivity (ρ_a) is defined as

$$\rho_a = \frac{1}{2\pi\mu f}\left|\frac{E_x}{H_y}\right|^2$$

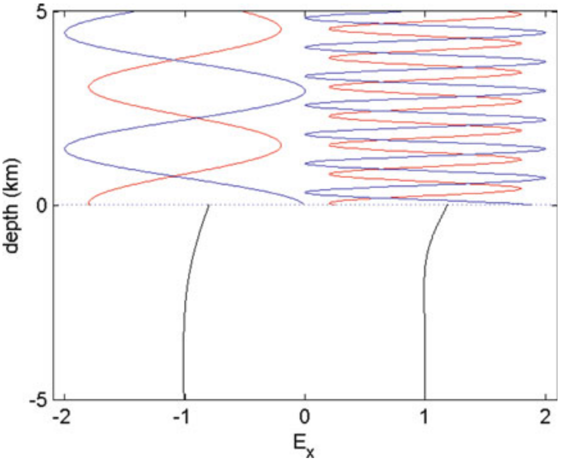

Fig. 13.7 Schematic diagram showing how the magnetotelluric method measures the resistivity of the Earth. A low frequency electromagnetic wave is incident on the Earth's surface (*blue*). Most of the energy is reflected (*red*) but a small proportion is transmitted into the Earth (*black*). The mode of propagation in the Earth is by diffusion. Note that the lower frequency signal penetrates deeper into the Earth than the high frequency signal. An animated version of this can be found at http://www.ualberta.ca/~unsworth/MT/MT.html

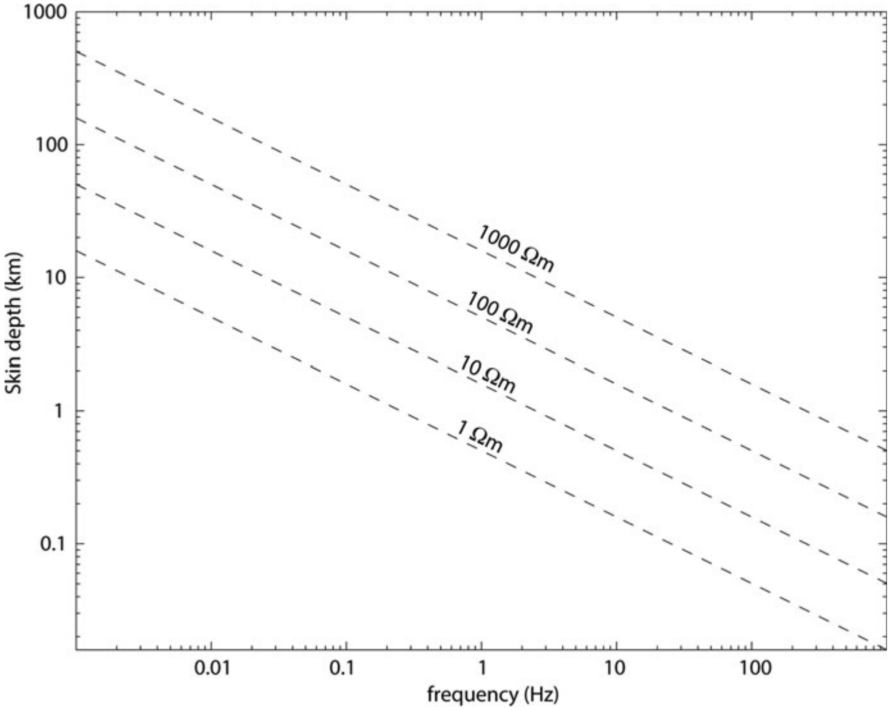

Fig. 13.8 (**a**) Skin depth (δ) as a function of frequency for uniform halfspaces with conductivity of 1,000, 100, 10, and 1 Ωm

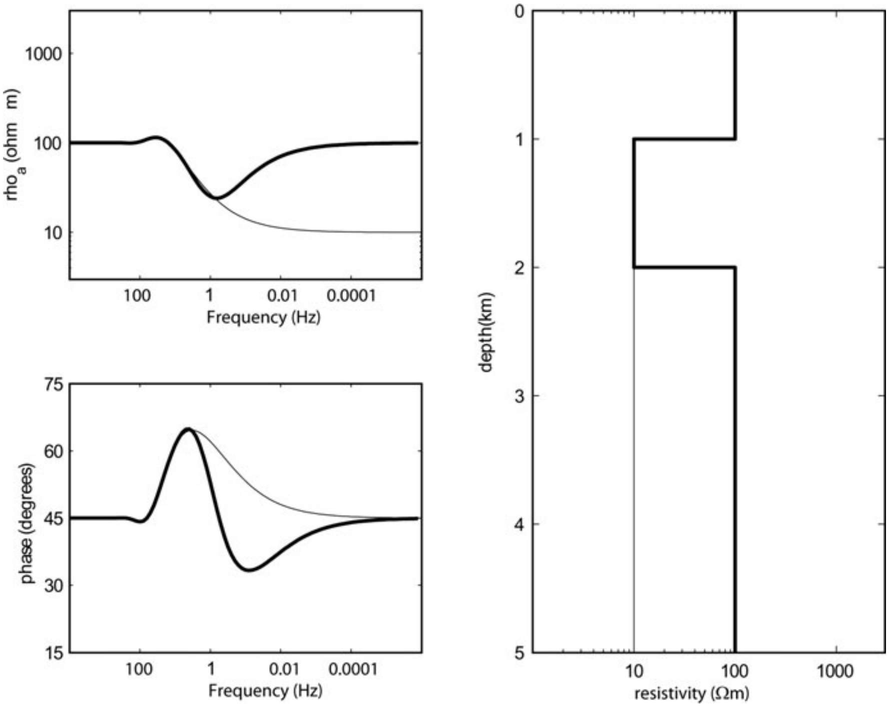

Fig. 13.9 Apparent resistivity and phase that would be measured at the surface over a 2-layer and 3-layer resistivity model

The apparent resistivity represents an average resistivity from the surface to a depth equal to the skin depth, δ. μ is the magnetic permeability, usually taken to be the free space value. Note that this only requires surface measurements of the electromagnetic fields to image resistivity at depth. More details of the MT method are described by Unsworth (2010).

13.2.2.1 MT Responses of a Layered Earth

The resistivity of the Earth usually varies with depth, so the equation for apparent resistivity is rarely applicable. To understand how MT can measure depth variation of resistivity, consider the case of a two-layer resistivity model shown in Fig. 13.9 (thin line). This will show how the measured apparent resistivity is related to the subsurface resistivity structure. In Fig. 13.9, the apparent resistivity is plotted as a function of signal frequency. Note that frequency decreases to the right, which corresponds to increasing depth of penetration in the Earth. At the highest frequencies ($f > 100$ Hz), the EM signals are attenuated before they ever reach the interface at a depth of 1 km. Thus, the apparent resistivity is the average resistivity over the region in which the EM signals travel, which is equal to the true resistivity of the upper layer (100 Ωm).

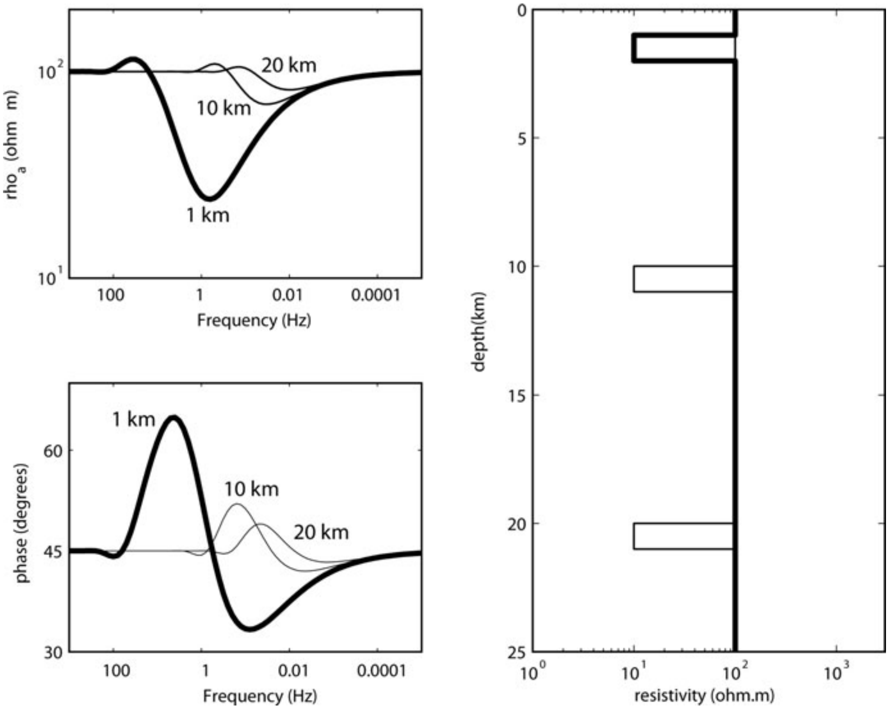

Fig. 13.10 Apparent resistivity and phase measured at the surface for a three layer Earth. The *top of the conductive layer* moves from 1 to 20 km depth. Note that as the layer moves deeper, the response becomes smaller

As the frequency decreases, the skin depth increases and signals will sample the lower layer. At these frequencies, the apparent resistivity represents an average of the two layers and it decreases with decreasing frequency. In the model in Fig. 13.9, this occurs at f ~30 Hz. As the frequency is further decreased, the skin depth increases and the depth of penetration becomes much greater than the layer thickness. This means that the apparent resistivity is dominated by the resistivity of the lower layer and the apparent resistivity asymptotically approaches the value of the lower half space resistivity (10 Ωm). The plot in Fig. 13.9 also shows the magnetotelluric phase. This quantity is the phase difference between the electric and magnetic fields and is sensitive to changes in resistivity with depth.

Figure 13.9 also shows a 3-layer model (thick line) with an increase in resistivity at a depth of 2 km. Note that apparent resistivity, as a function of frequency, shows a qualitative similarity to the variation of true resistivity with depth. In this model the second layer (1–2 km depth) can be considered a conductor, which is a relative term.

Figure 13.10 shows a set of 3-layer resistivity models where the depth to the top of the layer increases. This illustrates another important aspect of MT exploration

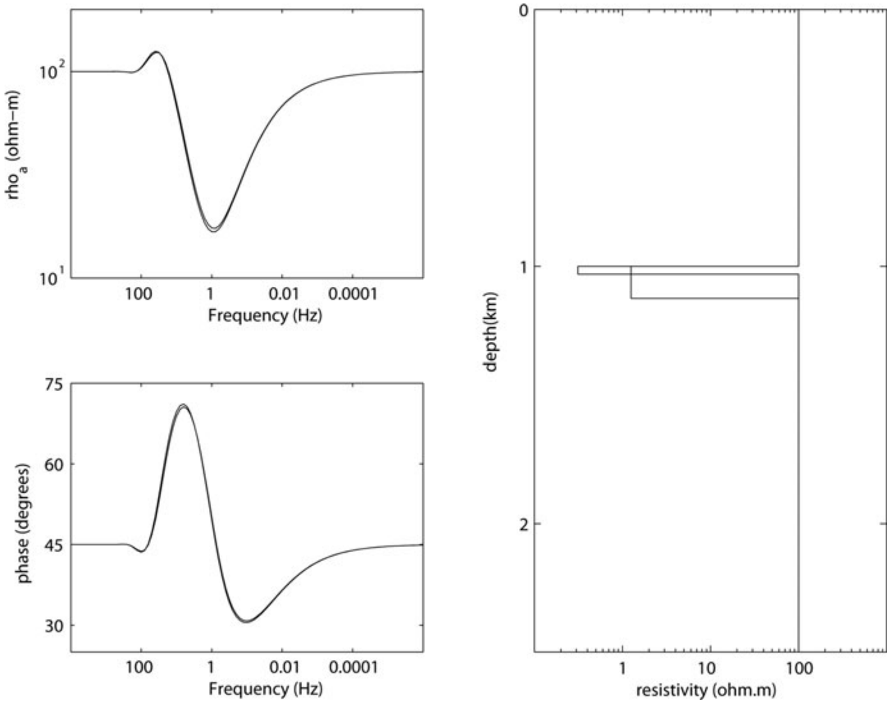

Fig. 13.11 Apparent resistivity for two resistivity models with a conductive layer at a depth of 1 km. Both models have the same conductance and give a very similar apparent resistivity and phase response

since it shows that the effect of a conductive layer on surface measurements becomes smaller as the depth of the layer increases.

The final example of MT responses illustrates a very important concept, as shown in Fig. 13.11. This figure shows a pair of resistivity models, each with a conductor at 1 km. The layers all have the same conductance, which is defined as the product of conductivity and thickness. In this example the conductance is 100 S. Note that the MT apparent resistivity curves are virtually identical for all models. Consider now the case of interpreting MT data collected over an unknown structure. With even a small amount of noise in the data, it would not be possible to distinguish between these models.

Comparing Figs. 13.10 and 13.11 shows both the ability and limitations of MT data to image the geometry and properties of conductive layers in the Earth. Remember that conductors, or zones of low resistivity, are typically associated with zones of aqueous fluids. MT is sensitive to the depth to the top of the layer and also to the conductance of the layer. However, MT cannot separately determine the thickness and conductivity of the layer. This should not be seen as a limitation of the MT method. Rather by understanding exactly what can be resolved with MT will allow it to be used more effectively.

13.2.2.2 MT Responses of 2-D and 3-D Earth Structures

The examples above show how a 1-D resistivity model can be investigated with MT. Most MT data are not 1-D and show aspects of 2-D and 3-D subsurface resistivity structure. Over a 1-D Earth, the same apparent resistivity will be measured regardless of the direction in which the electric and magnetic fields are measured. However, if the Earth has a 2-D resistivity structure, then the apparent resistivity will vary with azimuth. In the case of a location where the subsurface resistivity varies in 2-D, it can be shown that electric current parallel and perpendicular to the strike direction are independent (so called TE and TM modes). A number of tests can be applied to MT data to determine if 2-D analysis is appropriate. If a 2-D approach is appropriate, then 2-D inversion can be applied to a profile of stations using a number of well-tested inversion algorithms that will run quickly on a desktop computer (Rodi and Mackie 2001). A number of 2-D inversion models are presented later in this chapter. If the subsurface is characterized by a 3-D resistivity model, then a grid of MT stations may be needed to accurately define the structure. Inversion of such a dataset is much more computationally demanding than in the 2-D scenario and a number of algorithms are now available (Siripunvaraporn et al. 2005).

13.2.3 Magnetotelluric Data Collection

MT instruments are passive and record time variations in the Earth's magnetic field (H_x, H_y, H_z) and horizontal electric field (E_x, E_y). As described earlier, the skin depth phenomenon means that deeper investigation requires that lower frequencies are measured. For shallow exploration of the upper crust, instruments using induction coil magnetometers can be used to record data in the frequency range 1,000–0.001 Hz (so called broadband magnetotelluric instruments, available from commercial manufacturers). The system layout is sketched in Fig. 13.12. Broadband MT data collection typically requires 1–2 days recording per station. Deeper investigation uses long-period MT (LMT) with a fluxgate magnetic sensor and provides data in the frequency range 1–0.0001 Hz. Additional details about MT field techniques and data analysis are described by Simpson and Bahr (2005) and Unsworth (2010).

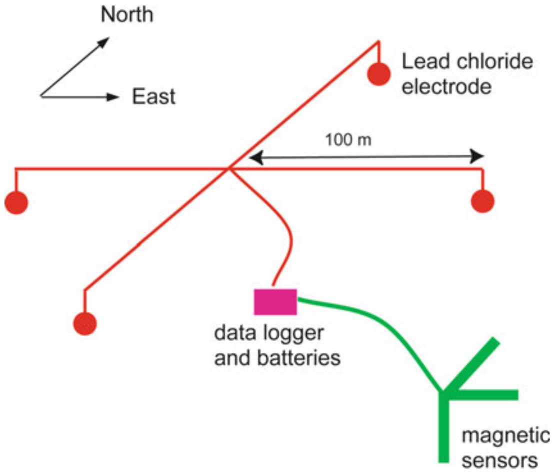

Fig. 13.12 Typical setup for broadband MT data collection. Electric fields are measured with a pair of dipoles that are connected to the Earth with non-polarizing electrodes. Magnetic fields are measured with induction coils that are buried to prevent motion

13.3 Seismic Methods

13.3.1 *Variations of Seismic Properties as a Function of Fluid Content, Hydration Alteration and Water in Anhydrous Minerals*

This section reviews the effects of metasomatism on seismic properties and observables. Once again, we treat metasomatism in the most general framework. That is, we take it to denote any form of interaction between water and minerals or rocks. In this framework, water can either be present as a free fluid in fractured and/or porous media, as structurally bound water (H_2O) or hydroxyl (OH) in hydrous minerals, or as H point defects in the structure of nominally anhydrous minerals. All of these occurrences of water change the response of materials to seismic waves that travel through them.

Relevant seismic observables discussed in this section include:

1. The velocities of compressional (P) waves, V_p, and shear (S) waves, V_s. In the crust and upper mantle, rocks have average velocities that range between 3.2–4.9 km/s for V_s, and 5.8–9.1 km/s for V_p (Dziewonski and Anderson 1981). Lower velocities can be found in parts of the uppermost crust that are weathered and/or fractured.
2. The Poisson's ratio, ν (sometimes also denoted by the symbol σ), which is the ratio of transverse contraction strain to the longitudinal extension strain in the direction of an applied stretching force. Typical values of Poisson's ratio for crustal and upper mantle rocks range between ~0.10 and 0.40 (Christensen 1996). The Poisson's ratio is related to V_p and V_s, or the V_p/V_s ratio, through the following expression: $\nu = 0.5[1-1/((V_p/V_s)^2 - 1)]$. An average value of

$\nu = 0.25$ = Poisson Solid ($V_p/V_s = 1.732$) is often considered typical for crustal and upper mantle rocks.

3. The seismic impedance, which is the product of seismic velocity and density, $I_p = \rho V_p$ for P-waves, and $I_s = \rho V_s$ for S-waves. The reflection coefficient at sharp seismic interfaces is proportional to the seismic impedance.
4. Seismic attenuation, which denotes the loss in seismic energy due to anelastic effects and scattering. Attenuation is defined by the quality factor $Q = 2\pi E/\Delta E$, or its inverse Q^{-1}, where ΔE represents the loss of seismic energy per unit cycle and E denotes the elastic energy stored in the system. Estimated values of Q, for the crust and upper mantle, range between the lowest values of ~30–40 for Q_S (S-wave attenuation) in the asthenosphere to values of several thousands in low-attenuation regions (e.g., Cammarano and Romanowicz 2008).
5. Seismic anisotropy, which is manifested by a variation in seismic velocity as a function of the propagation/polarization direction of seismic waves travelling though a given material. Anisotropy is commonly associated with the preferential orientation of fractures or mineral fabric. The magnitude of anisotropy is measured by taking the normalized difference between the maximum and minimum velocities for a given type of seismic wave, $(V_{max}-V_{min})/V_{mean}$, and can range from several percents to tens of percents depending on the mineral or mineral aggregate (Mainprice and Ildefonse 2009).

As we will discuss below, there exist two main approaches to determine the effects of water on seismic properties of materials: laboratory measurements and theoretical methods. We rely on results from these approaches to give an overview of how seismic properties are modified by hydrous fluids, hydrous minerals, and water in nominally anhydrous minerals.

13.3.1.1 Hydrous Fluids

As the term indicates, hydrous fluids refer to volatiles (in our case H_2O or aqueous solutions) in liquid form that occupy the voids present throughout a host rock. This situation is relevant to our discussion as the circulation of these fluids often stems from, or leads to, the occurrence of metasomatic reactions. It leads to the coexistence between a material that is porous and/or fractured (the matrix) and a fluid that fills its open spaces. This affects the seismic properties of subsurface materials in several ways when compared to dry, unfractured rocks. First, the presence of open fractures can reduce the stiffness of the rock. This effect is amplified when pore pressure is increased relative to confining pressure. Second, seismic energy may be absorbed through fluid displacement. The presence of interstitial fluid in fractured rocks at depth can thus have the following effects on seismic properties: a decrease in seismic velocities (V_p and V_s); a modification of the Poisson's ratio (or V_p/V_s ratio) of the composite material; an increase in the attenuation of seismic waves; and anisotropic behaviour if the fluid is present in fractures that are preferentially oriented.

Methodologies for Quantifying Physical Properties

Many approaches have been used to estimate the effects of porous fluids on the seismic properties of fractured materials. These can be grossly categorised into theoretical, numerical, and experimental approaches. They represent an active field of research, in large part driven by hydrocarbon exploration. Here, we provide a brief summary of these approaches, and we will discuss their results and their solid Earth implications in the next section.

Theoretical methods use thermodynamic and mechanical principles to establish relationships between elastic parameters and state variables that describe the fractured medium, e.g., fracture/pore density, geometry of the voids, properties of the solid matrix and the pore fluid. They include methods based on (1) effective medium theory, such as self-consistent approaches, which consider the minimum energy state at solid-solid and solid–liquid interfaces (e.g., O'Connell and Budiansky 1974, 1977; Schmeling 1985); and (2) poroelastic theory, which is based on continuum mechanics and seeks to estimate the seismic response of composite materials by linearly integrating the effects of the various components (see, e.g., Berryman 1995 for a review).

Numerical approaches seek to determine the effects of porous fluids by modelling a seismic wavefield propagating though materials containing predetermined asperities and fluid properties. For example, Hammond and Humphreys (2000a, b) used a finite-difference approach to look at the effects of partial melts on seismic velocities and attenuation for various pore shapes and concentrations.

Experimental methods measure seismic properties on samples of natural or synthesized rocks. Measurements on saturated porous rocks have been conducted largely in the context of hydrocarbon reservoirs, but the results can be easily extrapolated to deeper crustal rocks (see, e.g., Murphy 1985; Winkler and Murphy 1995, and references therein). Christensen (1984) made some measurements, specifically on oceanic basalts, to further characterize the effects of pore-fluid pressure on seismic properties. Constraints on the effects of water at greater depths in the lower crust and uppermost mantle (e.g., in subduction environments) can also be deduced from experiments on samples placed under high pressure-temperature conditions to investigate the effects of melt and/or fluids at the grain interface (e.g., Gribb and Cooper 2000; Aizawa et al. 2008).

Effects on Seismic Properties

Given the wide range of approaches described above and their various results, it is difficult to formulate a unified description of how aqueous liquids affect seismic properties. That is, there is no single expression or graph that can summarize the relationship between values of water content and seismic properties (e.g., velocities, attenuation, or anisotropy). Still, a generalisation of these results shows that an increase in water content has the following effects: (1) it tends to

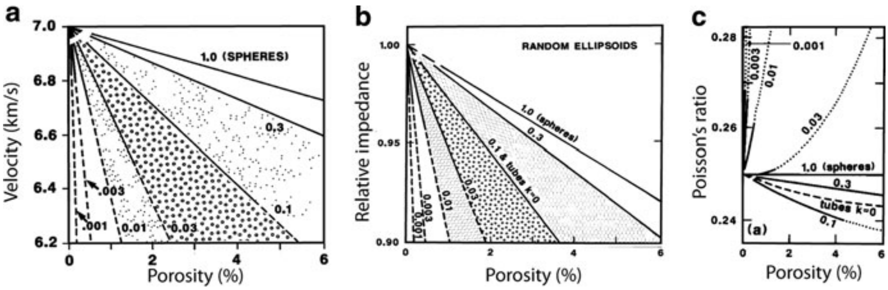

Fig. 13.13 Effects of porous fluids on seismic velocities for porosities ranging between 0% and 6% and pore aspect ratios (ratio of short to long axis) between 1.0 and 0.001. (**a**) P-wave velocity. (**b**) P-seismic impedance, relative to the unfractured (zero porosity) medium. (**c**) Poisson's ratio (Figures are from Hyndman and Klemperer (1989), and Hyndman and Shearer (1989))

reduce the stiffness of the rock, thereby reducing seismic velocities; (2) depending on the aspect ratio of the fractures/voids, it can either increase or reduce the Poisson's ratio (or V_p/V_s ratio); (3) it can increase the attenuation of seismic waves; and (4) it can cause seismic anisotropy. In the remainder of this section, we highlight some notable results that will help put some numbers on these general statements.

The perturbation in seismic velocities and V_p/V_s ratio associated with water-filled fractures is well summarized in papers by Hyndman and Shearer (1989) and Hyndman and Klemperer (1989), which seek to explain the high reflectivity and low velocities observed in the lower continental crust by controlled-source seismic investigations. These papers use the self-consistent approach described in Schmeling (1985) to calculate variations in V_p, seismic impedance I_p, and Poisson's ratio as a function of various pore aspect ratios (ratio of short to long axis), for rocks that are saturated with liquid water and porosities in the range 0–6%. Their results, which are summarized in Fig. 13.13, show that increased porosity systematically decreases the velocities, and that this effect is exacerbated as the pore aspect ratio becomes smaller, i.e., for long disk-shape voids that become equivalent to a network of thin, water-filled fractures (Fig. 13.13a). Since both V_p and density decrease with increased porosity, equivalent trends are observed for seismic impedances, noting that relatively small liquid fractions can cause impedance contrasts in excess of 5% relative to unfractured material – something that may yield important seismic reflections. Finally, while both V_p and V_s decrease systematically with increasing concentration of porous water, the Poisson's ratio (or V_p/V_s ratio) takes on different trends depending on the fractures' aspect ratios and the differential pressure (i.e., confining pressure minus pore pressure). It stays constant or decreases for aspect ratios between 0.3 and 1, and increases for smaller aspect ratios where thin water-filled fractures can preferentially reduce the resistance to shear. Experimental results indicate that these effects (reduction in V_p, V_s, and increase in V_p/V_s ratio) are amplified when pore pressure is increased relative to a constant confining pressure (Christensen 1984).

Three processes can lead to the attenuation and dispersion of seismic waves in saturated porous media: grain boundary sliding, liquid squirt between contiguous connected pores or fractures, and bulk fluid displacement (O'Connell and Budiansky 1977; Winkler and Murphy 1995; Wiens et al. 2008). Theoretical and numerical analyses suggest that the first two processes have relaxation time scales (i.e., range of frequencies where attenuation is maximum, between the unrelaxed and relaxed states) that are significantly higher than the central frequency of common seismic waves for both passive and active source applications (Hammond and Humphreys 2000a; Wiens et al. 2008). On the other hand, recent experimental results suggest that the first and third processes, grain boundary sliding and bulk fluid displacement, may cause attenuation in the frequency range of seismic waves, although the magnitude of these effects is still poorly constrained (see, e.g., Aizawa et al. 2008; and Wiens et al. 2008, and references therein for a review).

Aligned, fluid-filled fractures cause P and S seismic waves whose particle motion is in the plane of the fractures to travel faster than those whose particle motion is perpendicular to that plane, thus resulting in seismic anisotropy (see, e.g., Crampin and Booth 1985; Dunn and Toomey 2001; Fouch and Rondenay 2006). The magnitude of the anisotropy depends on the density of aligned fractures and on the combined properties of the solid and the fluid. A larger fracture density increases anisotropy, whereas the properties of the fluid control the overall bulk modulus of the medium. A formal theoretical treatment of the effects of fluid-filled cracks on seismic anisotropy is presented by Berryman (2007). These results show that such fractured media can have anywhere between several percent to tens of percent V_p and V_s anisotropy.

13.3.1.2 Hydrous Minerals

Hydrous minerals comprise water as part of their standard chemical structure. They are highly relevant to our discussion on metasomatism because they are both a main source of water carried and fluxed into the upper mantle by subduction zones, and a product of metasomatic alteration (see, e.g., Hyndman 1988; Hyndman and Peacock 2003; Grove et al. 2006; Chen et al. 2009). They tend to exhibit lower seismic velocities and higher seismic anisotropy than associated dry phases due to the inherent weakness of H bonds in their chemical structure and to the sheeted structure common to many species. Hydrous minerals can also cause seismic attenuation, though this effect is still poorly constrained (see, e.g., Pozgay et al. 2009). Here, we will discuss common hydrous minerals that are stable at relatively low temperatures in the crust and/or lithospheric upper-mantle, such as amphiboles, lawsonite, chlorite, and serpentine. We will also discuss accessory minerals associated with alteration reactions (e.g., talc and brucite), as these can produce highly anomalous seismic properties. Lastly, we will briefly discuss high-pressure hydrous phases (e.g., alphabet phases) that have the potential to carry water at great depth in the mantle transition zone and the lower mantle.

Methods for Quantifying Physical Properties

Once again, there exist three categories of approaches used to estimate the effect of hydration/alteration on the seismic properties of minerals and rocks: experimental measurements, theoretical calculations, and hybrid methods.

Experimental approaches are conducted either on natural and synthetic rock samples that are subjected to pressures and temperatures representative of conditions at depth (e.g., Birch 1960; Christensen 1966, 1984, 2004; Ito 1990; Kono et al. 2007), or on single crystals (e.g., Kumazawa and Anderson 1969; Frisillo and Barsch 1972; Schilling et al. 2003; Hilairet et al. 2006). Theoretical approaches, on the other hand, seek to estimate the elastic constants of hydrous minerals through first-principles quantum mechanical calculation (e.g., Reynard et al. 2007; Mainprice et al. 2008), or through atomistic simulations based on semi-empirical interatomic potentials that reproduce the structure of minerals (e.g., Auzende et al. 2006). Hybrid methods combine these two approaches, using experimentally-derived seismic properties of single minerals to compute the properties of rocks at depth. The mineral properties are extrapolated to high P-T conditions with thermodynamic equations, then combined with mixing laws to represent the desired assemblage (e.g., Bina and Helffrich 1992; Helffrich 1996; Hacker et al. 2003a).

Effects on Seismic Properties

Over the last 50 years, experiments and calculations have been conducted on many hydrous mineral and mineral assemblages to characterise their seismic properties. Due to the large quantity of material published on this topic over the years, it is not possible to review all of these results here. Thus we will focus the discussion on a few key results that pertain to hydrous minerals or rocks that play an important role in the context of subduction zones, as these represent the main point of entry of water into the Earth's mantle. Specifically, we will investigate the properties of the secondary alteration minerals serpentine and chlorite, as well at those of hydrated oceanic basalts. For more complete reviews, readers are referred to papers by Christensen (2004), Hacker et al. (2003a, b), and especially Mainprice and Ildefonse (2009).

The first two hydrous minerals that we shall discuss are serpentine and chlorite, which are common alteration minerals of lithospheric rocks. Serpentine is most commonly found as the hydrous alteration product of mantle peridotites, with peridotites transforming entirely into serpentinite and accessory minerals (e.g., talc, brucite, magnetite) if enough water is available, e.g. in saturated conditions. The formation of chlorite, on the other hand, is associated with the alteration of pyroxenes, amphiboles, and biotite, and is limited by the availability of Al in the crust and uppermost mantle. The top panels of Fig. 13.14 show the phase diagram of a hydrated lherzolite (a variety of peridotite) and the seismic properties corresponding to its various phases as a function of pressure and temperature (P-T)

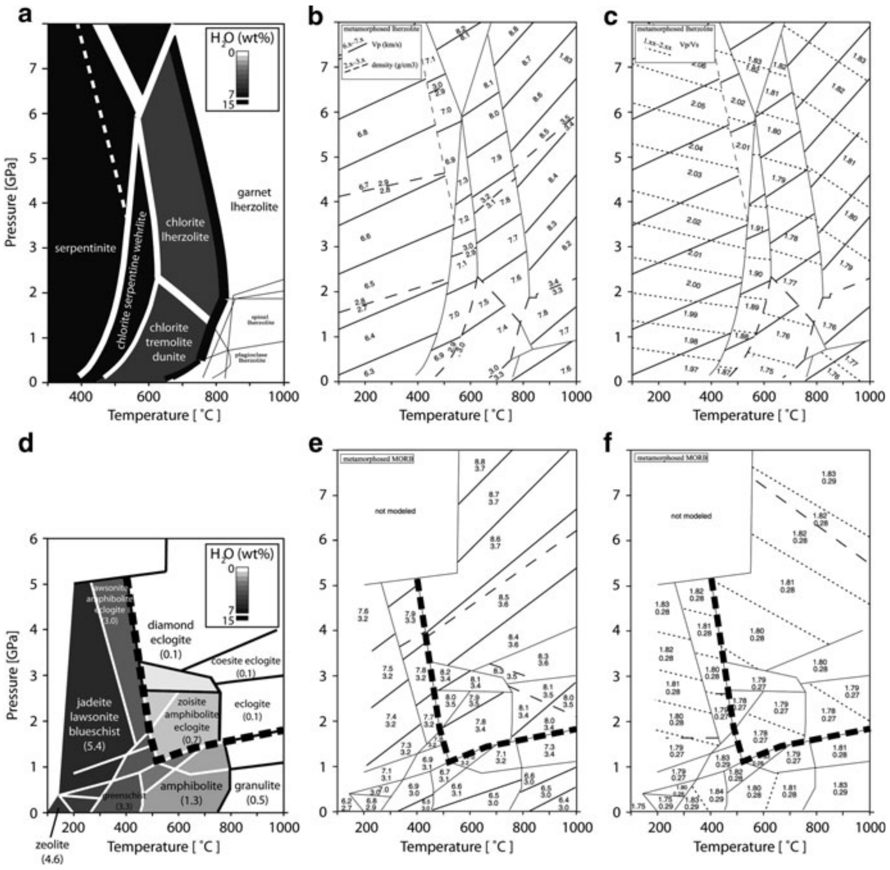

Fig. 13.14 Phase diagrams of hydrated rocks and their seismic properties as a function of pressure and temperature, calculated by the method of Hacker et al. (2003a). *Top row*: Phase diagram of lherzolite (**a**), with corresponding P-wave velocities and densities (**b**), and V_p/V_s ratios (**c**). *Bottom row*: Phase diagram of hydrated mid-ocean ridge basalt (**d**), with corresponding velocities and densities (**e**), and V_p/V_s and Poisson's ratio (**f**). The *thick dashed line* in panels (**d–e**) denotes the transformation into eclogite (Figures are modified from Hacker et al. (2003a))

conditions. These diagrams were obtained with the hybrid method of Hacker et al. (2003a) and outline the P-T conditions under which serpentine and chlorite are stable. We note that as the pressure increases, the water content of the rock decreases and that this decrease is accompanied by sharp, localised increases in seismic velocities and decreases in V_p/V_s ratio. The results of Fig. 13.14 are consistent with constraints obtained by experimental measurements, such as those of Christensen (2004) for antigorite (see Fig. 13.15), which is the variety of serpentine containing 13.0 wt.% H_20 that remains stable at the highest temperatures (see also, Hilairet et al. 2006).

Because of their layered structure, the alteration minerals serpentine, chlorite and their associated accessory minerals exhibit strong seismic anisotropy. Theoretical

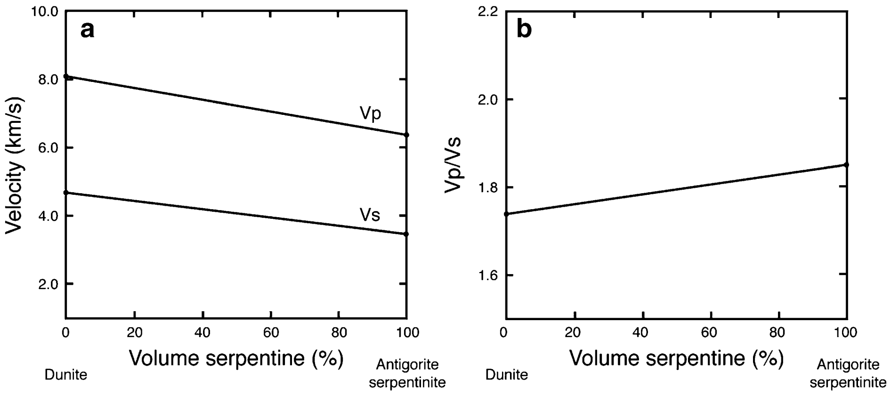

Fig. 13.15 Experimental results showing variations in (**a**) seismic velocities and (**b**) Vp/Vs ratio as a function of the degree of serpentinization, for the antigorite form of serpentine (Modified from Christensen 2004)

calculations for single minerals and experimental measurements on mono-mineralic aggregates have provided valuable estimates of anisotropic properties for several hydrous minerals (see Mainprice and Ildefonse 2009, and references therein). These include antigorite (71% V_p, 68% V_s), clinochlore and chlorite (35% V_p, 76% V_s), and talc (65% V_p, 68% V_s). Such large values suggest that strong seismic anisotropy may be observed for parts of the lithosphere and upper mantle that have undergone extensive hydrous alteration. However, this will only be the case if the hydrous minerals in real rocks exhibit a preferred crystallographic orientation when deformed under in situ P-T conditions, such that the bulk anisotropy is strong enough to yield detectable signals (e.g., Christensen 2004). Although the existence of such preferred orientation remains an open question, a handful of experimental studies, conducted on serpentine, have shown that crystals do indeed tend to align when aggregates are subjected to stresses similar to those found at convergent margins (Kern et al. 1997; Katayama et al. 2009; Bezacier et al. 2010a).

The second type of mineral assemblage we shall discuss is hydrated metabasalt, which is one of the main constituents of the oceanic crust and thus a major source of fluid input in subduction zones (see, e.g., Hacker et al. 2003a; Rondenay et al. 2008). At near surface P-T conditions, the main hydrous minerals in these rocks are chlorites and zeolites, which give the rock a ~5% H_2O content by weight. At intermediate P-T conditions, where chlorite remains stable, a significant portion of the mineral-bound water is also carried by amphiboles, which have been shown to exhibit strong seismic anisotropy (see, e.g., Bezacier et al. 2010b), and by lawsonite. The evolution of the water content and seismic velocities of hydrated metabasalts with increasing P-T conditions, as calculated by Hacker et al. (2003a) is shown in the bottom panels of Fig. 13.14. We observe that the water content progressively decreases with increasing P-T until the eclogite-facies is reached. We also observe that phase transformations are associated with significant changes in seismic properties. In particular, the transformation from lawsonite, blueschist, or granulite into eclogite translates into seismic velocity increases of up to ~12% Though these transformations do not necessarily occur at a precise subduction depth, as demonstrated by field observations of ultra-high pressure rocks (e.g., Austrheim et al. 1997), we may still be able to observe them in the seismic response. Note, also, that since they do not take into account the effects of pore-fluid pressure, the graphs of Hacker et al. (2003a) should be used with caution when interpreting seismic images of crustal segments that are potentially overpressured (see, e.g., Shelly et al. 2006; Audet et al. 2009).

We conclude this section on hydrous minerals by briefly discussing the stability of the minerals already discussed, which are generally stable to depths of ~200 km, as well as those that remain stable to much greater depths. The latter include the following minerals (see reviews in Williams and Hemley 2001; and Mainprice and Ildefonse 2009): clinohumite, which can be stable to mantle transition zone depths; hydrous ringwoodite and hydrous wadsleyite, both of which are found in the mantle transition zone; and dense hydrous magnesium silicates of the so-called alphabet series such as phase A (stable in the upper mantle), superhydrous phase B (stable in the transition zone), and phase D (stable to lower mantle depths). The seismic properties of many of these high-pressure phases have only been calculated theoretically, and generally exhibit small to moderate deviations from the properties of anhydrous mantle rocks (see, e.g., Mainprice and Ildefonse 2009). Even if some of these phases could remain undetectable by virtue of their seismic properties, they may still play an important role in the nucleation of deep earthquakes in subduction zones – another important seismic observable. Indeed, the dehydration reactions of hydrous minerals carried in cold subducted slabs (e.g., serpentine, chlorite, and lawsonite at shallow and intermediate depths; clinohumite, phase A, and superhydrous phase B at greater depth) are believed to trigger intraslab earthquakes. Another possible cause of intraslab seismicity is the rapid transformation of metastable, dry granulite to eclogite by additions of hydrous fluids (see, e.g., Jackson et al. 2004). In these models, earthquakes are caused by changes in the stress field related to densification reactions and/or by a reduction in friction coefficients due to the flux of released fluids into existing fractures – processes that are generally described as dehydration embrittlement (see, e.g., Green and Houston 1995; Hacker et al. 2003b).

13.3.1.3 Water in Nominally Anhydrous Minerals

As pressure and temperature increase with greater depth, and away from cold anomalies caused by subducted slabs, it becomes less and less likely to encounter liquid water or hydrous minerals. Water may still be present in these environments, though, with the introduction of H^+ cations as point defects in the structure of nominally anhydrous minerals. This phenomenon produces a weak H. . .O atomic bond that enhances anelasticity, reduces velocities, and has the potential to modify the anisotropic parameters. In this section, we will discuss the effects of water in olivine, the main anhydrous mineral phase in the upper mantle.

Methods for Quantifying Physical Properties

The main approach used in quantifying the effects of H point defects in nominally anhydrous minerals is a combination of experimental and analytical methods. In experimental methods, samples comprising single crystals of olivine or olivine-rich aggregates are subjected to deformation under high P-T conditions to measure the rheological properties and the dominant crystal orientation (e.g., Jackson et al. 1992; Jung and Karato 2001). From these experimental results, one can derive analytical expressions relating seismic properties, in particular anelastic relaxation and seismic anisotropy, to the concentration of absorbed water (see, e.g., Karato 1995; Karato and Jung 1998; and reviews by Karato 2003, 2006).

Effects on Seismic Properties

The introduction of water as H point defects in nominally anhydrous minerals, in particular olivine at upper mantle P-T conditions, has two main effects on the seismic properties of mantle rocks: (1) enhancement of anelasticity, which in turn causes modification of seismic velocities, and (2) modification of the crystal preferred orientation in deformed aggregates, which causes a realignment of the principal axes of seismic anisotropy.

Anelastic relaxation occurs as a result of intragranular processes, whereby H enhances dislocation and diffusion creep. Through grain-boundary processes, H increases grain-boundary mobility (Karato 2003). These processes result in enhanced seismic attenuation Q^{-1}, which can in turn translate into velocity reductions through the following expression (Minster and Anderson 1981; Karato 2003):

$$V(\omega, T, P, C_{OH}) = V_{\infty}(T, P)\left\lfloor 1 - \frac{1}{2}\cot\left(\frac{\pi\alpha}{2}\right)Q^{-1}(\omega, T, P, C_{OH})\right\rfloor, \tag{13.1}$$

where $V(\omega, T, P, C_{OH})$ is the seismic velocity as a function of frequency ω, temperature T, pressure P, and concentration of water in the form of hydroxyl C_{OH}. $V_{\infty}(T,P)$ is the unrelaxed seismic velocity at infinite frequency, and α is a parameter that describes the frequency dependence of attenuation and has been shown experimentally to take values between 0.1 and 0.3. The attenuation dependence on water concentration follows the proportionality relationship (Karato 2003):

$$Q^{-1}(\omega, T, P, C_{OH}) \propto \exp\left(-\alpha\frac{H^*}{RT_{eff}}\right), \tag{13.2}$$

with

$$T_{eff} = T \cdot \xi, \tag{13.3}$$

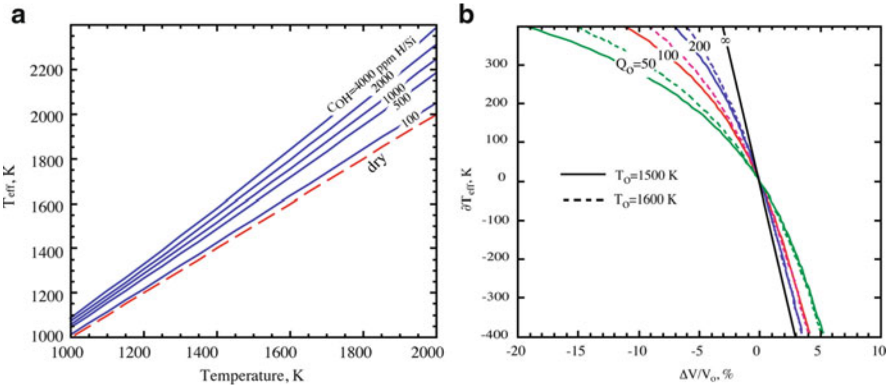

Fig. 13.16 Effects of water in nominally anhydrous minerals on seismic velocities. (**a**) Rheologically effective temperature, as a function of actual temperature, for various concentrations of water in olivine. (**b**) Velocity anomaly as a function of perturbation in rheologically effective temperature, for various values of the initial attenuation coefficient and temperatures (Q_0, T_0). For example, at $T_0 = 1{,}600$ K, the addition of 4,000 ppm H/Si (~0.03 wt.% water) raises the effective temperature by ~250 K (panel a), which can lead to a velocity perturbation of −3.2% for an initial (dry) attenuation coefficient Q_0 ~ 200 (panel b; see Karato 2003, his Fig. 13.2 for values of Q_0) (Figures are modified from Karato (2003))

and

$$\xi = \frac{1}{\left[1 - (RT/H^*) \cdot \log\left(A_w \cdot C_{OH}^r / A_d\right)\right]}, \tag{13.4}$$

where H^* is the activation enthalpy, R is the ideal gas constant, and T_{eff} is the rheologically effective temperature that incorporates the effects of water concentration through quantity ξ. The latter depends mainly on C_{OH} elevated to the power r, where r is an experimentally derived constant that depends on the process and takes on values between ~0.7 and 2.3 (see Karato 2006; his Table 1). Finally, A_w and A_d are constants that are independent of pressure and temperature (Karato and Jung 2003). Figure 13.16 illustrates these relationships. We see from the right panel of Fig. 13.16 that small concentrations of water (i.e., between 800 ppm H/Si and 3,000 ppm H/Si, which are reasonable estimates for typical oceanic asthenosphere and mantle wedge, respectively; see Karato 2003) are sufficient to generate seismic velocity perturbations of several percents.

Rheological experiments conducted on single crystals and aggregates of olivine have also shown that the addition of water causes the intragranular and grain-boundary effects discussed above to be enhanced along preferential crystallographic directions (e.g., Karato 1995; Jung and Karato 2001). Jung and Karato (2001) showed that these effects can have a dramatic effect on the deformation fabric of mantle olivines, as the crystallographic axis [001] becomes aligned with the maximum shear direction instead of axis [100] in dry samples. This leads to the existence of different types of olivine fabrics as a function of water concentration

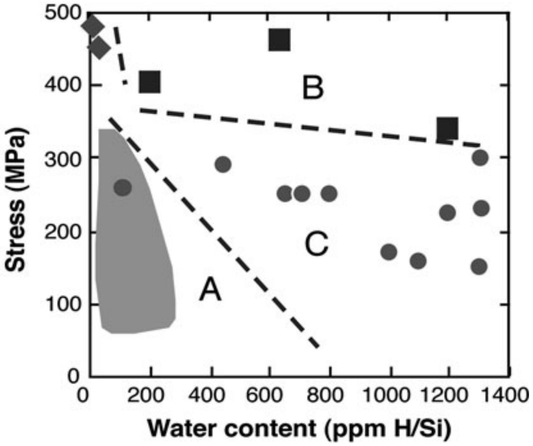

Fig. 13.17 Effects of water content and shear stress on the crystallographic orientation of olivine. *Symbols* and shaded area represent experimental results (see Jung and Karato 2001). *Dashed lines* define the fields corresponding to types A, B, and C fabrics. For a shear wave traveling perpendicularly to the shear plane, the fast polarization direction is parallel to the maximum shear direction in types A and C fabrics, while it is perpendicular to this direction in type B fabric. (Figure from Karato (2003))

and ambient shear stress (see Fig. 13.17). Type-A fabric corresponds to the most commonly assumed state for dry olivine, with its crystallographic axis [100] aligned subparallel to the shear direction and plane (010) subparallel to the shear plane. Type-B fabric is found for wet olivine under high shear stress conditions, and has its axis [001] aligned subparallel to the shear direction and plane (010) subparallel to the shear plane. Type-C fabric corresponds to wet olivine under low-stress conditions, and has its axis [001] aligned subparallel to the shear direction and plane (100) subparallel to the shear plane. One can fully appreciate the effects of these fabrics on seismic anisotropy when analyzing S waves that propagate perpendicularly to the shear plane (i.e., parallel to one of the crystallographic axes) and considering known elastic properties of olivine crystals (see, e.g., Babuška and Cara 1991). In this framework, S waves will observe a fast polarization direction parallel to the shear direction for types A and C. Conversely, for type-B fabric, the fast polarization direction will be perpendicular to the shear direction. There is, thus, a possible 90° ambiguity in the fast axis of anisotropy between dry and wet olivine aggregates.

13.3.1.4 Partial Melt

As discussed in Sect. 13.2.1, partial melt is directly linked to metasomatic processes. For example, melt alters the composition of rocks with which it comes in contact (including source rocks), rocks through which the melt migrates, and host rocks in which it crystallises. Moreover, melt can be caused by the addition of water to dry rocks and it can thus facilitate the transport of this water through the mantle and the lithosphere. Compositional variations due to partial melt extraction can cause observable changes in seismic properties, such as S-wave velocity perturbations of the order of 0.1 km/s for the range of values of Fe depletion in the source region of melts (e.g., Lee 2003). However, the main effects of partial melt are related to the viscoelastic response of the liquid–solid mixture (see, e.g., Wiens et al. 2008; and references therein). As such, the same approaches used to estimate the effects of water on observable seismic properties and to measure those in situ, which were described in Sect. 13.3.1.1, can be applied to liquid partial melt in a solid rock matrix. The pore space volume and geometry are defined by grain boundary topology, and they control the magnitude of seismic velocity and Q reduction. As in the case of aqueous fluids, experimental and theoretical methods suggest that melt fractions ranging between $\ll 1\%$ to several percent can produce large reductions in velocity and increases in attenuation (10s percent and more; see, e.g., Gribb and Cooper 2000; Takei 2002; Faul et al. 2004; Takei and Holtzman 2009a, b, c).

13.3.2 Seismic Methods for Imaging Fluids (Free and Mineral Bound) in the Deep Crust and Upper Mantle

After reviewing how seismic properties are affected by rock-water interactions, we now turn our attention to the seismic methods that are commonly used to observe these properties in situ, for rocks of the crust and upper mantle. We provide a brief discussion of each method that provides a qualitative understanding of the physical principles on which they are based and an appreciation of their resolving power.

13.3.2.1 Seismic Tomography

Tomographic approaches rely on the properties of transmitted seismic waves to produce images of volumetric seismic velocity anomalies (V_p, V_s) or seismic attenuation (Q_p, Q_s) of the subsurface. One of the most common tomographic approaches is based on the inversion of body-wave travel times to recover velocity variations (or perturbations) through a 3-D gridded volume (see, e.g., Nolet 2008 for a review of this and other approaches involving surface waves). Attenuation tomography, on the other hand, is performed by estimating attenuation parameters on individual ray paths by spectral analysis of P and S waveforms, and then inverting these data for Q perturbations through a 3-D grid (see, e.g., Stachnik et al. 2004). The reader should also be aware of recently developed techniques that yield improved resolution of subsurface structure, which include full seismic waveform inversion (e.g., Brenders and Pratt 2007; Tape et al. 2010), and tomographic methods based on the cross-correlation of ambient seismic noise (e.g., Shapiro et al. 2005).

Due in part to the inherent trade-off between smoothness and error misfit that characterises inverse approaches, tomographic images tend to produce spatially smooth images that are not particularly sensitive to sharp velocity boundaries. The spatial resolution of tomographic images can be defined as the smallest size perturbation that can be imaged accurately. It depends on a number of parameters such as the seismic ray coverage through the imaged volume (which in turn depends on the source and receiver coverage), the magnitude of the anomalies, and the frequency content of the seismic signal. For adequate coverage, the resolution is proportional to the quantity $\sqrt{\lambda \cdot l}$, where λ is the wavelength of the signal and l is the length of the ray.

Travel-time tomography approaches, that seek to image seismic structure in the crust and upper mantle at regional scales, can use controlled sources (e.g., long-range refraction/wide-angle profiles), local earthquake sources, or teleseismic sources. The spatial resolution afforded by P-wave models is of the order of a few km to 10s of kilometres for controlled source applications (depending on the source/receiver density and depth), ~10–35 km for local earthquake source applications, and ~50–70 km for teleseismic approaches.

13.3.2.2 Seismic Reflection

Seismic reflection is a controlled-source technique that relies on recordings of near-offset seismic body-waves that are reflected at sharp discontinuities in material properties in the subsurface. These recordings are corrected for differential travel-times as a function of offset and stacked to increase their signal-to-noise ratio. The signals are mapped to depth using a range of possible techniques involving varying degrees of sophistication (from simple 1-D time-depth conversions to more involved 2-D or 3-D back projection-migration operators) to form vertical profiles of seismic discontinuities of the crust and uppermost mantle. The strength of the imaged reflectors is proportional to the seismic impedance contrasts at the discontinuities and to the thickness of the discontinuities, i.e., where a discontinuity can either be perfectly sharp or gradational over a finite thickness. Spatial resolution can thus be defined, here, as either the maximum gradient thickness that a discontinuity must have to produce an observable reflection, or as the minimum separation for two perfectly sharp discontinuities to be distinguishable. A commonly used rule of thumb suggests that this quantity is of the order of λ/4, though complete separation between two discontinuities is achieved at λ/2, where λ is the wavelength of the signal (see, e.g., Levander et al. 2006). For a typical frequency range of ~10–50 Hz in crustal seismic studies, the value of λ for P-waves ranges between ~508 and 116 m in the upper crust (for $V_p = 5.8$ km/s), ~700–140 m in the lower crust (for $V_p = 7.0$ km/s), and ~810–162 m in the upper mantle (for $V_p = 8.1$ km/s).

13.3.2.3 Passive-Source Converted and Scattered Wave Imaging

Methods in this section exploit the phenomenon of scattering and conversion of teleseismic waves at sharp discontinuities of the subsurface. They are similar to reflection methods in the type of structure they image, but complement these methods in terms of their probing depth since they illuminate the structures from below instead of from the surface. Another key difference is that these passive imaging techniques rely principally on P-to-S converted waves in the coda of P-waves (and also on S-to-P conversions in the percusory signal of S waves) to identify discontinuities. As in the case of reflection imaging, the recorded traces are source-normalised and stacked to increase the signal-to-noise ratio. The mapping to depth is done either in 1-D below single stations or array of receivers, in an approach commonly referred to as receiver function (RF) imaging, or using back-projection migration operators that can image structures in 2-D and 3-D below arrays of receivers (see, e.g., Vinnik 1977; Langston 1979; Dueker and Sheehan 1997; Bostock and Rondenay 1999; Levander et al. 2006; and for a review, see Rondenay 2009). In their applications to direct imaging, these approaches produce profiles highlighting discontinuities from the lower crust to the mantle transition zone. The amplitude of these signals is more sensitive to rapid changes in V_s than to density perturbations, as the latter have more influence on reflection coefficients than on transmission coefficients (see, e.g., Rychert et al. 2007). Spatial resolution is defined in the same way as in reflection seismic, though with a value that is now twice as large ($\lambda/2$ rather than $\lambda/4$) given that the process involves transmission instead of reflection (see Rondenay 2009). The maximum frequency of signals analysed is typically between 0.3 and 1.5 Hz, yielding spatial resolutions of ~6.7–1.3 km in the lower crust ($V_s = 4.0$ km/s), and ~7.8–1.6 km in the uppermost mantle ($V_s = 4.7$ km/s). RF signals can also be inverted to obtain layered velocity models of the crust (Ammon et al. 1990), and for estimating the average Poisson's ratio of the crust (Zhu and Kanamori 2000).

13.3.2.4 Shear-Wave Splitting Analysis

This category of approaches is used to characterize seismic anisotropy in the subsurface. It exploits the phenomenon whereby shear waves, that travel through anisotropic media, are split into two quasi-S waves that are polarized along the principal axes of anisotropy and thus travel at different velocities – a phenomenon similar to optical birefringence (for reviews on the topic see Silver 1996; Savage 1999; and Fouch and Rondenay 2006). Shear-wave splitting analysis consists of applying an operator to split shear waves recorded at the surface (commonly S and SKS waves) to recover the directions of the principal axes of anisotropy and the strength of the anisotropy. The method generally assumes hexagonal anisotropy with a horizontal axis of symmetry, and returns two parameters: the azimuth of the fast polarization axis ϕ, and the time shift between the two split waves δt, which is representative of the strength of anisotropy (product of percent anisotropy and thickness of the anisotropic layer). Values of anisotropic parameters are usually given for single stations using multiple events. The lateral resolution below the stations is defined by the Fresnel zone of the seismic rays that are analysed (e.g., 90 km radius at 120 km depth of a vertically incident SKS wave with 12 s dominant period; see Fouch and Rondenay 2006). Conversely, the method is insensitive to the depth extent and vertical position of the anisotropic layer, since it measures a path-integrated process. It is still possible to obtain constraints on the depth of anisotropy, though. This is done, for example, by interpreting shear-wave splitting results in conjunction with surface waves sampling a region of interest from various azimuths (see, e.g., Chen et al. 2007).

This completes our review of the resistivity and seismic properties of crustal and upper mantle rocks that can detect fluids that cause metasomatism in the Earth. We now proceed with case studies that will illustrate the applicability of geophysical approaches to detect metasomatism in different geodynamic environments.

13.4 Mid-Ocean Ridges

Hydrothermal circulation of seawater causes extensive serpentinization of the newly formed oceanic crust at the global mid-ocean ridge system. It has been estimated that this causes a 20–30% volume increase (Bach and Früh-Green 2010). Hydrothermal circulation within the oceanic crust at a mid-ocean ridge has been imaged with EM geophysical data, primarily using a system of transmitters and receivers. Hydration of the ocean plate also occurs as it bends and enters a subduction zone. Seismic imaging of faulting has defined this process in Central America and shown that the fluids circulate deep enough to hydrate both the oceanic crust and the mantle (Ranero et al. 2003). Magnetotelluric profiles collected onshore and offshore Costa Rica have imaged the deep circulation of the hydrothermal fluids (Worzewski et al. 2010).

13.5 Subduction Zones

Subduction zones are important in the global tectonic cycle because of their role in transporting fluids from the surface of the Earth into the crust and upper mantle. This provides a link between the Earth's hydrosphere, lithosphere, and biosphere. The significance of fluids in controlling the properties and evolution of the lithosphere cannot be overstated (Wannamaker 2010). Water is transported in the subducting plate as both (1) free water within sediments and the ocean crust and (2) as hydrated minerals in the oceanic crust (e.g., amphiboles) and in the upper mantle (e.g., serpentine; see Fig. 13.18). This water is released in the subduction zone over a depth range that extends from the surface to at least 200 km (Hyndman

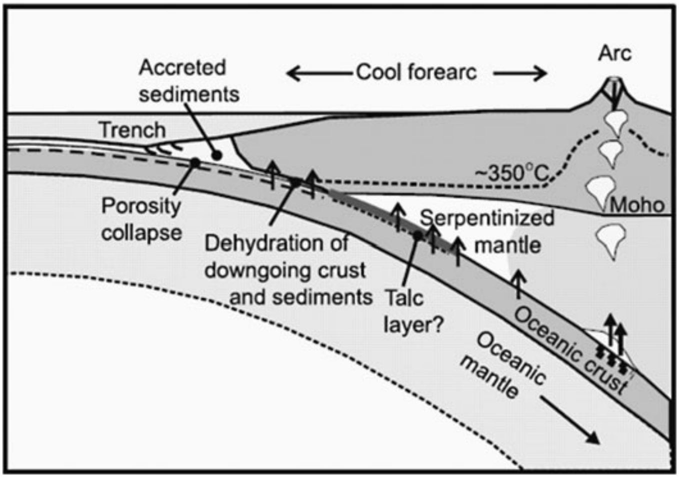

Fig. 13.18 Schematic of fluid flux in a subduction zone, based on Fig. 13.1 from Hyndman and Peacock (2003)

and Peacock 2003). Some recent studies suggest that significant water may be transported as far as the mantle transition zone (Bercovici and Karato 2003; Booker et al. 2004)

This release of fluids controls the processes that occur in the subduction zone. For example compression of the seafloor sediments causes porosity collapse that expels water as the accretionary wedge develops. Deeper in the lithosphere, increasing temperature and pressure in the downgoing slab drives prograde metamorphic reactions that generate fluids (e.g. basalt to eclogite in the slab, plus others). These fluids migrate upwards and can cause retrograde metamorphic reactions in the colder part of the mantle wedge, e.g. addition of water to the mantle wedge converts peridotite into serpentinite. The release of water at greater depths (i.e., ~100 km) causes a lowering in the melting point of the mantle and triggers melting that supplies the volcanic arc. This is a key part of the mechanism that has led to the development of a felsic crust and the presence of continents on the surface of the Earth (O'Neill et al. 2007).

Geophysical imaging has played a significant role in the development of the view of subduction zones summarized above. This is because the presence of fluids can change the seismic velocity and electrical resistivity of rocks. Seismic and magnetotelluric surveys have contributed in two distinct ways: (1) they are able to detect fluids within a subduction zone, and (2) they can also detect the changes that occur in rocks as they undergo metamorphism. These geophysical studies have also allowed the first steps to be made towards quantifying the rate of fluid flux into the lithosphere (Hyndman and Peacock 2003). The Cascadia subduction zone is one of the best studied subduction zones in the world and will be the focus of this section. References to studies of other subduction zones are included to keep the discussion as general as possible.

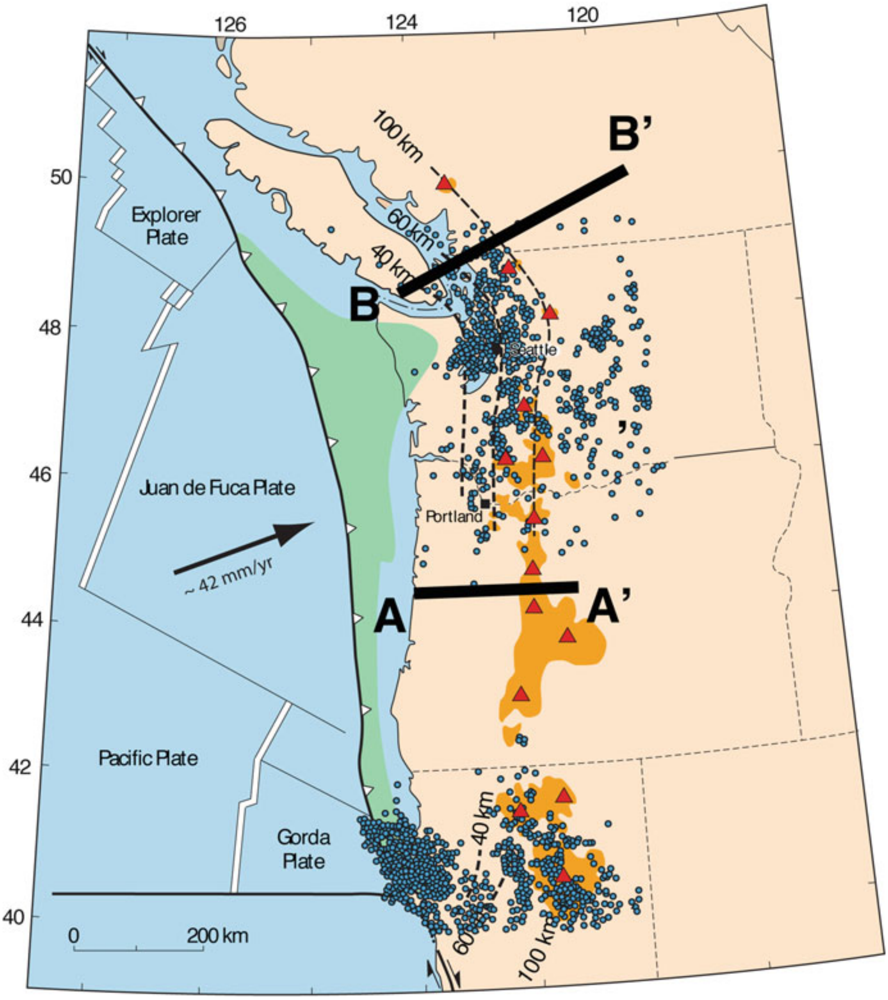

Fig. 13.19 Simplified tectonic map of the Cascadia subduction zone. Line A-A' and B-B' indicate the location of geophysical profiles discussed in the text. *Blue circles* denote earthquakes and *red triangles* indicate the locations of Quaternary arc volcanoes. (Figure is modified from Romanyuk et al. (1998))

13.5.1 Tectonic Setting and Geophysical Studies of the Cascadia Subduction Zone

The Cascadia Subduction Zone (CSZ), which is shown in Fig. 13.19, extends along the west coast of North America, from southern British Columbia to northern California. In the CSZ, the Juan de Fuca plate subducts beneath North America at a rate of 35–45 mm/year in a NE direction (DeMets et al. 1994). Along the trench, the subducting plate is very young (i.e., 6–10 Million year; Wilson 2002), placing it at the warm end of the spectrum of plate thermal structures (Hacker et al. 2003b; Hyndman and Wang 1993; Kirby et al. 1996). It is among the youngest subducting plates on the planet to produce a continuous volcanic arc, with Quaternary volcanoes that extend along nearly the entire length of the subduction zone. A Wadati-Benioff zone is observed between 40 and 90 km depth in the northern CSZ, north of 47°N, suggesting a slab dip steepening from 10° to 30° in that region. Conversely, intra-slab seismicity is conspicuously absent in Oregon for reasons that are not well understood (e.g., Wells et al. 2002). Yet, active volcanism, magnetotelluric analyses and seismic images support the existence of a dehydrating slab that is continuous to at least 150–200 km depth beneath the central CSZ (e.g., Rasmussen and Humphreys 1988; Wannamaker et al. 1989; Rondenay et al. 2001). Below, we briefly summarize the types of MT and seismic investigations that have been undertaken across Cascadia over the last three decades.

Kurtz et al. (1986, 1990) presented one of the first MT studies of a subduction zone with a profile crossing southern Vancouver Island. Though it yielded compelling evidence for the existence of fluid-rich zones in the system, it has been shown that such MT onshore data may be strongly influenced by the presence of nearby oceans, as these are the largest conductors found on the surface of the Earth. Thus, MT profiles that combine both onshore and offshore MT data, such as the one discussed below, have the potential to image onshore resistivity structures more reliably than a profile with just onshore data (Evans et al. 2002).

The EMSLAB project was the first major effort to apply magnetotellurics to study a subduction zone from the oceanic plate to the continental interior. The survey used an east–west transect in central Oregon that was more than 1,000 km long. Wannamaker et al. (1989) described the resistivity model derived by forward modelling both the onshore and offshore MT data (see Fig. 13.20). Since the Vancouver Island and EMSLAB studies from the 1980, new images of the Cascadia subduction zone have been published by several authors (Aprea et al. 1998; Vanyan 2002). This has included the first long-period MT data capable of imaging the lower crust and upper mantle of the Cascadia Subduction zone across southern British Columbia (Soyer and Unsworth 2006; see Fig. 13.21). Previous studies used only broadband MT data that were limited in the depth of penetration.

Cascadia has been studied seismically using a wide variety of approaches, including imaging with off-shore and on-shore controlled source data, and analyses of broadband data from permanent stations or dense networks. Controlled-source studies provide images of seismic discontinuities and volumetric anomalies in the 0–50 km range. They have been conducted across the accretionary wedge and forearc mantle wedge in southern British Columbia (Green et al. 1986; Clowes et al. 1987; Calvert 1996, 2004), Washington state (Flueh et al. 1998; Preston et al. 2003), and in Oregon (Tréhu et al. 1994). Other controlled-source transects were designed to investigate the volcanic arc (e.g., Leaver et al. 1984; Tréhu et al. 1994; Miller et al. 1997). Regional 3-D velocity models, based on active-source and local earthquake data, have provided detailed crustal structure across large portions of the Cascadia subduction zone (Parsons et al. 2005; Ramachandran et al. 2006).

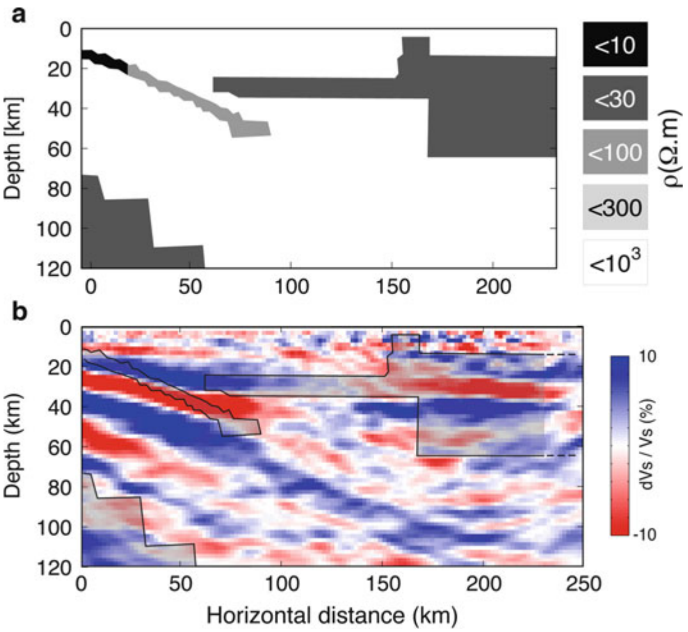

Fig. 13.20 Comparison of MT and seismic results across central Oregon – profile A-A' in Fig. 13.19. (**a**) Resistivity model derived from forward modelling of MT data recorded as part of the EMSLAB project (Wannamaker et al. 1989). (**b**) Seismic discontinuity profile derived from inversion of teleseismic scattered waves (Rondenay et al. 2001). *Shaded* area indicates the projection of conductive features superimposed on the seismic image

Broadband seismic studies have yielded tomographic velocity models of the entire Cascadia subduction zone between 0 and 400 km depth (Rasmussen and Humphreys 1988; VanDecar 1991; Bostock and VanDecar 1995; Zhao et al. 2001; Xue and Allen 2007; Roth et al. 2008), and high-resolution profiles of seismic discontinuities in the 0–150 km range across southern British Columbia, Washington and central Oregon (Rondenay et al. 2001; Nicholson et al. 2005; Abers et al. 2009). Individual broadband stations have also been used to analyse velocity and anisotropy structure beneath the region (Langston 1977, 1979; Cassidy and Bostock 1996; Park et al. 2004).

13.5.2 Subducted Crust and Slab Dehydration

The MT study of Kurtz et al. (1986, 1990) revealed an eastward dipping zone of low resistivity beneath southern Vancouver Island that was inferred to represent the uppermost part of the subducting Juan de Fuca Plate. The low resistivity zone was coincident with a dipping set of reflectors, the E-horizon of Green et al. (1986). Active source seismic studies have shown that both the low resistivity layer and

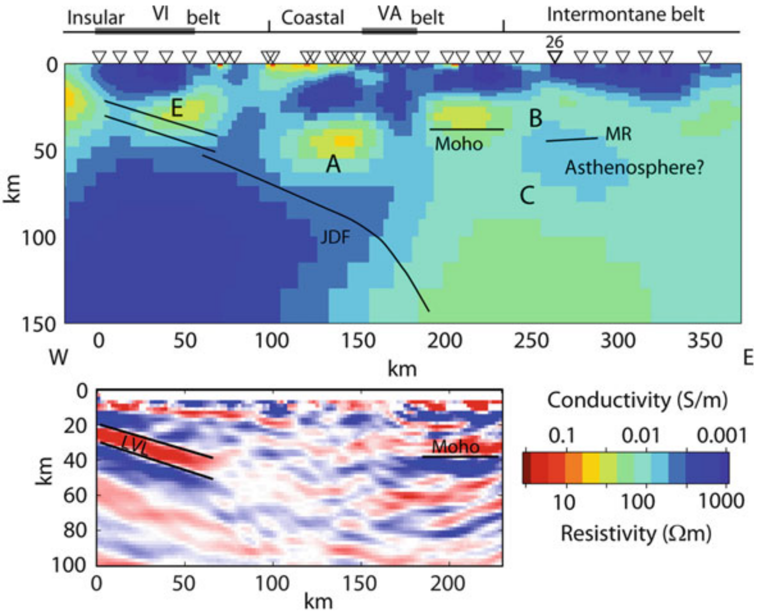

Fig. 13.21 Comparison of MT and seismic results across southern British Columbia – profile B-B' in Fig 13.19. (**a**) Resistivity model for Cascadia Subduction Zone derived from inversion of the magnetotelluric data (Soyer and Unsworth 2006). (**b**) Seismic discontinuity profile derived from inversion of teleseismic scattered waves (Nicholson et al. 2005). *Black lines* in both panels show the interpretation of imaged features

reflectors are located in the overriding North American Plate some 10 km above the subduction thrust in the crust, reflecting fluids derived from the Juan de Fuca Plate that are trapped by an impermeable layer at a temperature of around 400°C (Hyndman 1988). The observed resistivity can be explained by a 1–2% porosity filled with saline fluids. A debate has continued about the exact origin of the E-horizon with Calvert and Clowes (1990) proposing it to be a shear zone associated with subcreted sediments because the fluids alone could not explain the strength of the reflections.

At the regional scale, recent high-resolution seismic profiles based on teleseismic scattered waves suggest that the subducted crust is represented by a thin, low-velocity layer that extends from ~20 km depth beneath the coast to ~40 km depth beneath the forearc basin (Rondenay et al. 2001; Nicholson et al. 2005; Abers et al. 2009). The spatial extent of this low-velocity layer appears to coincide with dipping conductive structures detected by Wannamaker et al. (1989) in central Oregon (see Fig. 13.20), and by Soyer and Unsworth (2006) in southern British Columbia (see Fig. 13.21). Note that in each figure, both the low-velocity layer and the dipping conductor appear to terminate where the Juan de Fuca plate comes in contact with the mantle wedge. These results have raised new questions about the exact location of the dipping electrical features, but regardless of whether

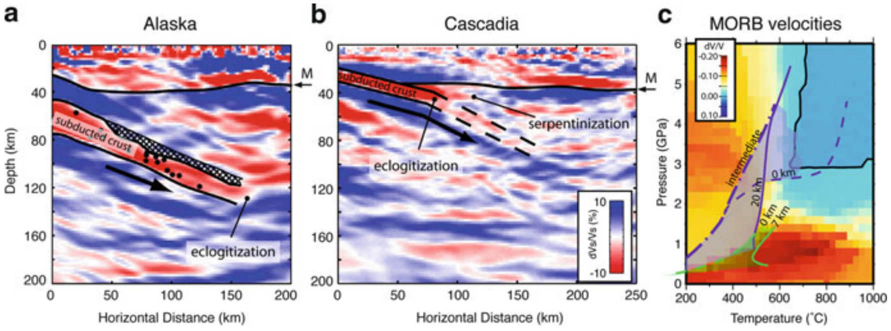

Fig. 13.22 Seismic imaging of slab dehydration reactions. Comparison between seismic profiles of (**a**) an older, thus cooler subducted slab in southern Alaska, and (**b**) a younger, thus warmer subducted slab in Cascadia. (**c**) Estimated P-T paths of both subducted crusts (Cascadia in *green*, Alaska in *purple*) superimposed on velocity perturbations of metamorphosed mid-ocean ridge basalts (MORB). The P-T paths are calculated by running geodynamic models, and denote temperatures at the subduction interface (*dashed lines*), the subducted Moho (*solid line*), and, for Alaska, the depth of minimum crustal temperature (*dash-dot line*). Velocity perturbations are estimated following Hacker and Abers (2004), and Hacker (2008). They are slightly different than the plots described in Sect. 13.3.1.2 because a different approach is used to calculate mineral modes (Figures are modified from Rondenay et al. (2008))

the conductive layer is situated at the top of the subducted slab or above the subduction interface, it is clearly the product of progressive dehydration of the subducted oceanic slab. Our first concern is thus to address slab dehydration.

The spatial extent of slab dehydration has been inferred through (1) the mapping of intraslab seismicity (e.g., Hacker et al. 2003b; Rüpke et al. 2004; Brudzinski et al. 2007), (2) the characterization of low-velocity layers by waveform modelling (e.g., Abers 2005), and (3) direct seismic imaging (e.g., Rondenay et al. 2008). Although all these approaches provide important complementary constraints on this process, here we will focus on the last one. In their study, Rondenay et al. (2008) compared the seismic profiles of two thermally distinct subduction zones, Cascadia and Alaska, and used constraints from geodynamic and petrological models to interpret the seismic images in terms of dehydration reactions. They found that the low-velocity dipping layer is associated with hydrated basalts, that its termination can be explained by the transformation of these basalts into eclogite, and that the depth of this transformation is dependent on the thermal state (age) of the slab. Thus older, colder slabs (e.g., Alaska) possess subducted crusts that persist as low-velocity layers to much greater depths than those of younger, warmer slabs (e.g., Cascadia). Figure 13.22 shows a comparison between the two imaged slabs and their thermal state as a function of increasing P-T conditions. These results, which generally agree with those from other approaches mentioned above, indicate that high-resolution seismic profiling can image robustly where dehydration reactions take place.

13.5.3 Flux of Fluids into the Overriding Crust

As the subducting slab dehydrates, fluids flux into the subducting crust and potentially into the overlying portions of the subduction system. In regions where the slab is in direct contact with the overriding crust, fluids may thus form a channel that runs parallel to the interface – either above or beneath the interface. The dipping conductive layers mentioned in the previous section (Kurtz et al. 1986; Wannamaker et al. 1989; Soyer and Unsworth 2006) may represent a direct evidence of these channels. Recent seismic results have also shown evidence for such channels in the form of sharp seismic discontinuities across southern British Columbia and Washington state (e.g., Audet et al. 2009; Abers et al. 2009). As mentioned in the previous section, some authors have suggested that this channel is formed in the overriding crust above the subduction interface (e.g., Hyndman 1988). Conversely, the receiver function study of Audet et al. (2009), which detects a dipping layer with an anomalously high Poisson's ratio, suggests a layer of overpressured hydrous fluids trapped under a sealed plate boundary at the subduction interface. This channel would comprise the entire column of the subducted crust.

The existence of fluids, potentially trapped at the subduction interface, is believed to play an important role in the recently discovered process of episodic tremor and slip (ETS). ETS are recurrent bursts of non-volcanic tremors that are accompanied by aseismic slip events occurring down-dip of the locked segment of the subduction interface (see, e.g., Rogers and Dragert 2003). They have been observed in the subduction zones of Cascadia, Japan, Alaska, Mexico, and Costa Rica (Rogers and Dragert 2003; Obara et al. 2004; Peterson and Christensen 2009; Payero et al. 2008; Brown et al. 2009). Although their exact cause is still unknown, it has been widely believed since their discovery by Obara (2002), that tremors are related to the presence of free fluids in the vicinity of the subduction interface, i.e., fluid flux from the slab and/or high pore-fluid pressure in the subducted crust (e.g., Shelly et al. 2006; Audet et al. 2009). In this scenario, the tremors may be associated with the movement of fluids (e.g., hydrofracturing) or to a modification of the stress conditions at the subduction interface. The recent study of Abers et al. (2009) across Washington state clearly shows a direct correlation between the lateral (trench-normal) extent of the tremors and that of the dipping low-velocity channel at the top of the subducted slab. This result, in conjunction with a similar conductive structure inferred from MT, suggests that seismic and MT analyses can help directly image the source region of ETS.

13.5.4 Flux of Fluids into the Mantle Wedge

Down dip of the intersection between the top of the subducted slab and the base of the overriding crust, fluids are fluxed from the slab into the mantle wedge. In the upper corner of the mantle wedge, where temperatures are cooler, water-rich fluids cause alteration of mantle peridotites into serpentine and associated accessory minerals (see Sect. 13.3.1.2; and the review by Hyndman and Peacock 2003). At greater depth, in the warm circulating portion of the mantle wedge, the influx of water-rich fluids trigger partial melting of mantle peridotites by lowering their melting temperature (see, e.g., Grove et al. 2006). Here, we will focus on the effects of water on the hydration-alteration of the mantle wedge. For a comprehensive review about geophysical observation of magma distribution in subduction zones, the reader is referred to Wiens et al. (2008).

Kamiya and Kobayashi (2000) presented one of the first direct geophysical observations of serpentine alteration in the mantle wedge using P- and S-wave tomography across central Japan. They interpreted a localized region with a high V_p/V_s ratio (>0.3) in the corner of the mantle wedge (20–45 km depth) as being due to the presence of serpentinite. Similar observations were made soon after in Cascadia with tomographic models (Zhao et al. 2001), high-resolution profiles based on teleseismic scattered waves (Bostock et al. 2002), and controlled source seismic surveys (Brocher et al. 2003). These seismic results were further supported by the magnetotelluric study of Soyer and Unsworth (2006), who observe a low resistivity zone 'A' that was shown to be required by the data (see Fig. 13.21). Other magnetotelluric studies of subduction zones that revealed how fluids are transported to depth, then released to cause metamorphism include those in Mexico (Jodicke et al. 2006), and Costa Rica (Worzewski et al. 2010). Mantle wedge serpentinization can also be observed by potential field methods. For example, Blakely et al. (2005) suggest that the forearc mantle wedges in Cascadia and Alaska both exhibit negative gravity anomalies associated with serpentine, combined with positive magnetic anomalies due to magnetite, which itself is an accessory mineral of serpentinization.

In the Cascadia profiles, derived from teleseismic scattered waves, the presence of serpentine has been inferred from an anomalous response of the continental Moho (see Bostock et al. 2002). In most of these profiles, a clear Moho is observed on the east side of the sections with a characteristic increase in velocity from crust to mantle. However above the mantle wedge, an anomalous structure is observed with either a very weak Moho in southern British Columbia and central Washington (see Fig. 13.21 between model offsets of 70 and 170 km; see, also, Abers et al. 2009), or even a reversed polarity Moho in central Oregon (Bostock et al. 2002; see also Figs. 13.20b and 13.22b between 50 and 130 km model offsets). This implies that there is either a minimal or inverted velocity contrast between the crust and mantle, with the mantle here exhibiting anomalously low velocities. Brocher et al. (2003) notes that this same Moho behaviour is observed in the form of an absent or muted Moho reflection (P_mP) below refraction lines that sample the forearc along the entire length of the CSZ.

Bostock et al. (2002) used constraints from thermal models and petrological results to interpret this unusual Moho response as due to serpentine. First, thermal models show that the weak or inverted Moho is present directly above the portion of the mantle wedge where temperatures are below ~650°C, the maximum temperature at which serpentine is stable (see Sect. 13.3.1.2). Second, they show that an inverted Moho implies an upper-mantle S-wave velocity $\leq$3.25 km/s, which implies a level of serpentinization of 50–60% based on petrological results. Christensen (2004) later pointed out that these conclusions were based on measurements for lizardite, a lower temperature variety of serpentine. Instead, if one considers results for antigorite (the variety of serpentine stable at the highest temperature, see Sect. 13.3.1.2 and Fig. 13.14), velocities cannot be lowered to 3.25 km/s by serpentine alone and thus an additional mechanism is required, for example, high pore pressures (Christensen 2004).

A global compilation of seismic anisotropy measurements in subduction zones by Long and Silver (2008) suggests that the introduction of water in the cold corner of the mantle wedge may lead to observable type-B fabric (see Sect. 13.3.1.3). This process is manifested by a trench-parallel fast axis of seismic anisotropy observed in many subduction zones. Experimental measurements by Katayama et al. (2009) indicate that a trench-parallel fast axis can also result from crystal-preferred orientation of deformed serpentine in subduction zones characterized by steeply dipping slabs. However, in Cascadia the fast axis is trench-perpendicular in all portions of the system and appears to stem mainly from the response of the sub-slab asthenosphere to absolute slab motion (Currie et al. 2004); a somewhat unusual observation that may be associated to the exceptionally young age of the subducted slab (Long and Silver 2008).

In terms of MT response, serpentinite can locally lower the resistivity of crustal and upper mantle rocks, compared to unmetamorphosed peridotite. This resistivity reduction occurs mainly through increased porosity, with additional conduction occurring through mineral phases such as magnetite (Stetsky and Brace 1973). Thus the low mantle resistivity observed in the Cascadia mantle forearc requires the presence of aqueous fluids, associated with ongoing metamorphism. A simple estimation of the fluid content can be made with Archie's Law, provided that the pore fluid resistivity can be estimated. Nesbitt (1993) showed that crustal pore fluid resistivity is generally in the range 0.3–0.03 Ωm. However, it should be remembered that MT gives a robust constraint on conductance, not the individual conductivity and thickness that make up a given conductance. This is illustrated for a range of fluid resistivities and cementation factors in Fig. 13.23. As expected, the same conductance can be accounted for by a porosity that decreases as the layer thickness increases. This non-uniqueness can be addressed by noting that the thickness of the mantle wedge is defined by seismic constraints at around 20 km. The value of the cementation factor, m, is likely close to unity since saline fluids will be interconnected, giving Φ in the range 0.0002–0.002 depending on the value ρ_f chosen.

13.6 Metasomatism in the Stable Continental Lithosphere

The continental lithosphere is generally viewed as a dry environment, though mounting geological and geophysical observations suggest that some parts are or have been affected by circulating fluids. This is to be expected considering that

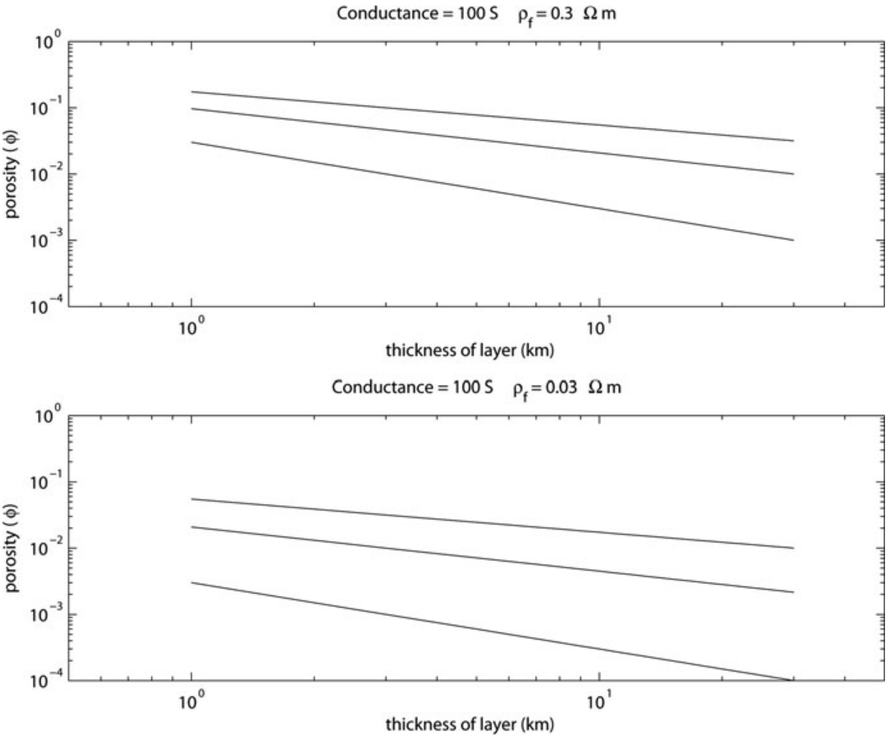

Fig. 13.23 Thickness and porosity combinations required to explain a 100 S conductor in the forearc mantle wedge. *Upper* and *lower* panels are for a pore fluid resistivity of 0.3 Ωm and 0.03 Ω m respectively. In each panel, the three curves are for cementation factors of m = 1, 1.5, and 2 in Archie's Law

subduction plays a key role in the formation of the continental crust and lithospheric mantle, both through arc volcanism and terrane accretion. Moreover, the introduction of fluids can be facilitated by post-stabilization events such as lithospheric delamination or plume interaction, as these place the lithosphere in contact with more fertile and hydrated mantle.

In this section, we will discuss the effects of water on the crust and lithospheric mantle. Instead of concentrating on one specific region, as we did in the previous section, we will focus the discussion on two main types of continental environments: (1) the lower continental crust, especially that of Phanerozoic age, which exhibits higher electrical conductivity and seismic reflectivity than the upper crust, and lower seismic velocities than those predicted by laboratory analyses of dry xenoliths; and (2) the lithospheric mantle of Archean cratons, which has been shown to contain regions of mineral alteration associated with the subduction-accretion events that played a role in their initial assembly.

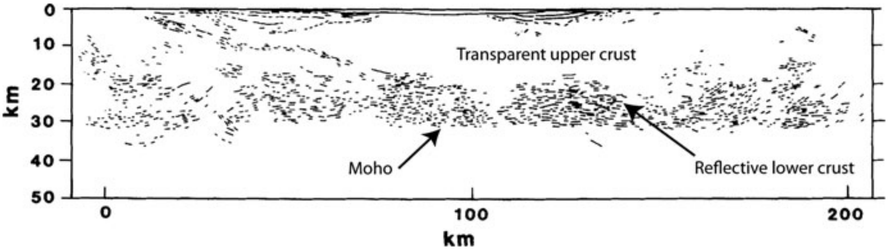

Fig. 13.24 Example of a seismic reflection profile across the southwest continental shelf of the British Isles, showing a reflective lower crust and a transparent upper crust (Modified from Matthews 1986)

13.6.1 Phanerozoic Crust

Phanerozoic crust is relatively young and formed in the last ~542 Ma. It is usually found along the periphery of continents, and is underlain by a lithospheric mantle of moderate thickness that transitions to asthenosphere at an average depth of ~100 km. Like all other types of continental crusts, Phanerozoic crust has been extensively studied by both geological and geophysical means. Geophysical observations have long found that the lower Phanerozoic crust was somewhat atypical in that it is characterized by a combination of (1) high electrical conductivity, (2) enhanced seismic reflectivity compared to the higher crust, and (3) lower seismic velocities than those predicted by experimental measurement on dry xenoliths. Here, we explore how these properties can be explained by the presence of fluids in the lower crust.

Through a compilation of MT observations, Hyndman and Klemperer (1989) observed that Phanerozoic lower crust has an average electrical resistivity of 20–30 Ωm, much lower than predicted values of 10,000–100,000 Ωm for dry lower-crustal rocks. They also noted that this average value is significantly lower than that for lower crust of Proterozoic and Archean ages (~500 Ωm); though from these observations, it is clear that most lower continental crust appears more conductive than laboratory measurements predict. Such low conductivities can be due either to interconnected porous fluids, or an interconnected conductive phase such as graphite (Jones and Ferguson 2001).

From a seismological standpoint, Phanerozoic lower crust exhibits two distinctive characteristics (Hyndman and Shearer 1989; Hyndman and Klemperer 1989). First, it is generally more reflective than the upper crust (see Fig. 13.24). It has been proposed that this is due to the presence of lenses rich in porous fluids (Hyndman and Shearer 1989; Suetnova et al. 1994); to a composition made of alternating metamorphic rocks with differing acoustic impedances (Christensen 1989); or to a combination of the two. Second, Phanerozoic lower crust has lower seismic velocities than those predicted by lab measurements made on mafic rocks (i.e., ~6.6–6.75 km/s compared to predicted velocities of >7.00 km/s; Hyndman and Klemperer 1989). This could be simply explained by assuming that Phanerozoic lower crust is composed primarily of intermediate composition rocks that exhibit lower seismic velocities. However, analyses of deep crustal xenoliths recovered at the surface tend to indicate a predominantly mafic composition (see Hyndman and Klemperer 1989; and references therein). Alternatively, the low velocities could be due to the presence of a fluid phase, i.e., either an aqueous fluid or a partial melt. Though since the temperatures are relatively low in the lower-crust of stable continental settings (lower than the vapour-saturated solidus), the most likely candidate here would be an aqueous fluid.

Although the electrical and seismic characteristics of Phanerozoic lower crust can be explained in several ways, the model that best explains all the observations is the presence of a saline aqueous fluid in interconnected pores. Calculations made by Hyndman and Shearer (1989) and Hyndman and Klemperer (1989), based on the effective medium theory implementation of Schmeling (1985), suggest that these observations can be explained by only 1–2% porous water. Their model considers water in intergranular pores as opposed to actual fractures, since an extensive network of open fractures is unlikely under high-pressure conditions corresponding to lower crustal depths. As seen in Sects. 13.2 and 13.3, the important parameters for estimating the electrical and seismic properties are the porosity, as well as the dihedral angle and aspect ratio of the pores. For their estimates, Hyndman and Shearer (1989) use an average dihedral angle of ~60°, Archie's Law exponents between 1.5 and 2, and pore aspect ratios of 0.03–0.1, all of which are based on experimental results. Thus, for an average resistivity of 20–30 Ωm, they find that a porosity of 0.5–3% is needed if the fluid has a salinity equivalent to that of seawater. As for seismic observations, impedance contrasts of 5–10% as those observed require 1–4% porosity (Hyndman and Shearer 1989; Fig. 13.13b), and velocity reductions of 5% can be explained by 1–2% porosity (Hyndman and Klemperer 1989; Fig. 13.13a).

As described above, possible fluid sources include dehydration from underlying subducted slabs or mantle devolatilization processes, which may inject fluids throughout the entire crustal column. This raises an important question, though, as to why these inferred fluids are confined to the lower crust. Hyndman and Shearer (1989) suggest that the minimum depth is constrained by a temperature of 350–400°C, which may mark an impermeable horizon formed by a hydration reaction (at the top of greenschist facies conditions) or silica precipitation. Porous water may thus remain trapped under this boundary over geological time. The fact that equivalent properties may not be found in Precambrian lower-crust is attributed to potential tectonothermal events that dehydrate the lower crust by prograde metamorphic reactions. However, relict metasomatism may still be found deeper in the thick lithospheric roots of Archean cratons as discussed in the next section.

13.6.2 Archean Cratons

Archean cratons often form the nuclei of Precambrian continental shields. They are generally thought of as highly stable entities whose longevity is attributed to the combined effects of their deep, coherent lithospheric roots (i.e., tectosphere, Jordan 1978) and the protection afforded by neighboring Proterozoic orogens (see, e.g., Lenardic et al. 2000, 2003). As in the case of the crust, water may be introduced into the cratonic lithosphere during its assembly and through alteration processes that occur after its stabilization.

Let us first consider the assembly stage. Geological and geochemical mapping of crustal lithologies suggest that Archean provinces were assembled through tectonic processes similar to, although perhaps more vigorous than, those that have been active during Phanerozoic times (see, e.g., Helmstaedt and Schulze 1989; Calvert et al. 1995; Albarède 1998, and references therein). Mechanisms invoked for their assembly include imbrication of island arcs and oceanic plateaus, and possible accretions to even older proto-cratonic nuclei (see, e.g., Ludden and Hubert 1986; de Wit et al. 1992; Albarède 1998). These mechanisms are driven by subduction. Thus water-rich fluid is introduced both by dehydration of the subducted slabs and by advection of hydrated terranes from the near surface into the deep structure of the lithosphere.

After their assembly and stabilization, some Archean cratons have experienced only limited reworking, such as kimberlite injection and/or local interactions with mantle plumes (e.g., Superior craton; Rondenay et al. 2000). Conversely, other cratons were deeply modified by large-scale events, such as lithospheric delamination (e.g., North China Craton; Gao et al. 2002). All of these alteration processes, whether local or regional, have the potential to inject water-rich fluids into the lithosphere by putting it directly in contact with more fertile/hydrated mantle that either replaces the delaminated lithosphere or intrudes it.

Given the involvement of water in processes of cratonic assembly and evolution, it is likely that signs of water circulation should remain visible in the cratonic lithosphere over geological time scales. Here, we discuss a recent geophysical study carried out in the Slave craton that supports this hypothesis. The Slave province is a small Archean craton located in the northwest corner of the Canadian Shield (Fig. 13.25). Exposed lithologies mainly comprise Late Archean (2.73–2.58 Ga) supracrustal and plutonic rocks, although the craton also hosts some of the oldest dated rocks on Earth, the ~4.03 Ga Acasta gneisses (Bowring et al. 1989, 1990). The Slave craton is flanked by two Proterozoic orogens, the Thelon orogen to the east and the Wopmay orogen to the west. The Slave craton is an attractive scientific target because it is well exposed and preserved, and because its underlying mantle is sampled by more than 150 kimberlite pipes (Heaman et al. 1997) that provide petrological constraints on the entire lithospheric column. The Slave craton has been the subject of extensive geophysical investigations (e.g., Bostock 1997, 1998; Bank et al. 2000; Jones and Ferguson 2001; Jones et al. 2001; Snyder et al. 2003,

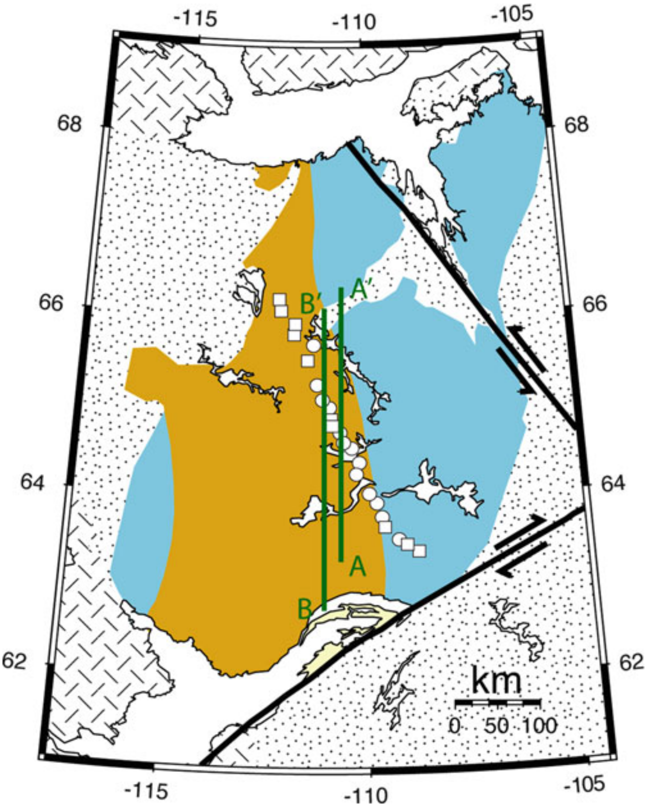

Fig. 13.25 Map of the Slave craton. *Color shaded* region denotes the exposed area of the craton, with *orange shading* showing the outline of the older Central Slave Basement Complex (4.03–2.83 Ga). *White squares* and *circles* denote seismic stations. *Black* solid lines are major faults. Projection lines of the seismic (A-A') and resistivity (B-B') profiles are indicated in *green* (Figure modified from Chen et al. (2009))

2004; Chen et al. 2007, 2009; Mercier et al. 2008). For the purpose of this discussion, we will focus on results from magnetotelluric and seismic receiver function studies.

Magnetotellurics studies of the Slave craton were among the first to clearly detect an electrical Moho, in the form of a sudden drop in resistivity from ~50,000 to ~5,000 Ωm occurring at 35.5 km depth (Jones and Ferguson 2001; Jones et al. 2001). According to Jones and Ferguson (2001), the enhanced visibility of the electrical Moho is attributed to the fact that the Slave Craton does not exhibit the conductive lower crust often found in other environments (see Sect. 13.6.1). This indicates that the crust here has probably been heated and dehydrated, as suggested by the hypothesis of Hyndman and Shearer (1989). Such resistive crust has the benefit of enhancing the sensitivity of MT data to the resistivity of

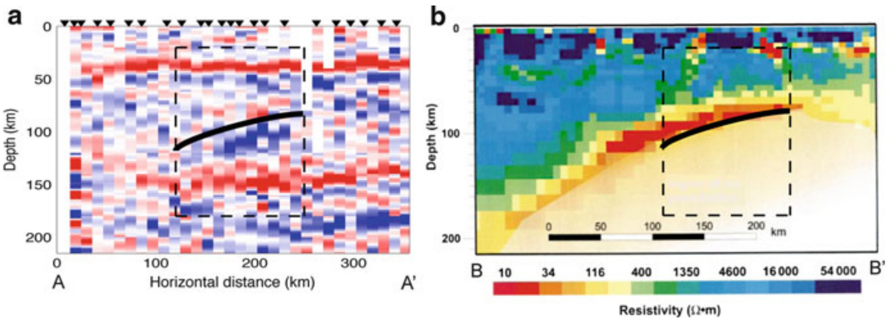

Fig. 13.26 Comparison of seismic and resistivity profiles across the central Slave craton. (**a**) Receiver function profile, *colour coded* such that *red*/*blue* represent positive/negative discontinuities in seismic velocities Vs, where a positive discontinuity represents a downward slow-to-fast transition, and a negative discontinuity represents a downward fast-to-slow transition. (**b**) Resistivity profile, with *colour scale* indicating values of electrical resistivity. See Fig. 13.25 for projection lines. The coincident seismic/electrical anomaly is indicated by a *thick black line*, in the area outlined by the *dashed box* (Figure modified from Chen et al. (2009))

the underlying mantle structures. This has allowed Jones et al. (2001) to image a strong, south-southwest dipping conductor, centred at ~100 km depth, in the cratonic lithosphere beneath the central Slave Craton. The transition from mantle rocks to the conductor marks a sharp reduction in resistivity from 1,000–10,000 Ωm to ~15 Ωm. According to these authors, the low resistivity layer is best explained by the presence of an interconnected conductive phase, most likely graphite.

In terms of seismic constraints, several recent analyses based on converted teleseismic waves and surface waves have shown evidence for a seismic discontinuity located at the same depth as the conductive anomaly described above (Chen et al. 2007, 2009; Moorkamp et al. 2007, 2010). In particular, the receiver function profile of Chen et al. (2009) images a dipping seismic discontinuity that overlaps almost exactly with the conductor detected by Jones et al. (2001). The seismic discontinuity marks a rapid decrease in seismic velocity (9–21%) with depth. A comparison of the two profiles is shown in Fig. 13.26.

In trying to interpret the coincident electrical and seismic anomalies, Chen et al. (2009) showed that they probably do not have a unique physical origin. Indeed, the most likely candidate would be the presence of a fluid or melt at depth, but P-T conditions at 100 km depth impede the prolonged existence of either fluids or melts. Instead, these authors suggest that the anomalies are related to the same process, metasomatism, but that different metasomatic alteration/deposition products cause the two anomalies. That is, hydrated minerals cause the seismic velocity reduction, and graphite causes the conductive anomaly. This hypothesis is supported by petrological analyses of mantle xenoliths sampling the anomalous region, which suggest that hydrous fluids were introduced at that depth and caused metasomatic alteration at the time of cratonic assembly (Aulbach et al. 2007). Relying on additional evidence from diamond ages, Chen et al. (2009) suggest that this metasomatic front is associated with a subduction event that took place during paleo-Archean time (~3.5 Gyr ago) and contributed to the assembly of the lithospheric block now forming the central Slave craton. The study of Chen et al. (2009) thus presents compelling evidence that relict metasomatism can be preserved over billions of years in the cratonic lithosphere, and that combined geophysical analyses can image the affected regions.

13.7 Fluids Generated in Collision Zones

Collision zones occur in a range of tectonic settings including continent-continent collisions and arc continent collisions. In both situations, the relative buoyancy of the continental crust prevents its subduction and a region of thickening crust develops.

In an arc continent collision, such as Taiwan, the buoyant continental crust does not enter the subduction zone and a region of thickened crust develops. In the crustal root, elevated temperature and pressure causes prograde metamorphic reactions that generate fluids. Mineralization provides evidence for past fluid flow in major fault zones (Lewis et al. 2007). Magnetotelluric studies have provided evidence that this fluid flow continues today with a major conductive zone detected beneath Central Taiwan and originating in the crustal root (Fig. 13.27 and Bertrand et al. 2009). Similar tectonic processes occur beneath the South Island of New Zealand and have also formed a crustal root. The magnetotelluric results of Wannamaker et al. (2002), shown in Fig. 13.27, also show evidence of fluid generation in the crustal root, with transport upwards to the surface. These fluids clearly cause metasomatism at higher crustal levels. In both these collision zones, upper crustal material is progressively buried, and then exhumed through erosion. It has been suggested that most of the fluids are generated beneath the Southern Alps as crustal material is being exhumed (Vry et al. 2010). Figure 13.27 shows that MT is a powerful tool for imaging the pattern of fluid generation beneath an active orogen in real time. Studies to the north in the Malborough sound area have shown how fluids may play a role in the development of the orogen (Wannamaker et al. 2009).

In a continent-continent collision, such as the India-Asian collision a large region of thickened crust has formed the Himalaya and Tibetan Plateau. In places this exceeds 80 km in thickness. Radiogenic heat production in the thickened crust causes prograde metamorphism and ultimately crustal melting (Beaumont et al. 2001). These melts can tunnel horizontally and form an interconnected layer extending over a horizontal distance for 100s of kilometres. Geophysical data has given the strongest evidence for this melt layer. Seismic reflection data showed that

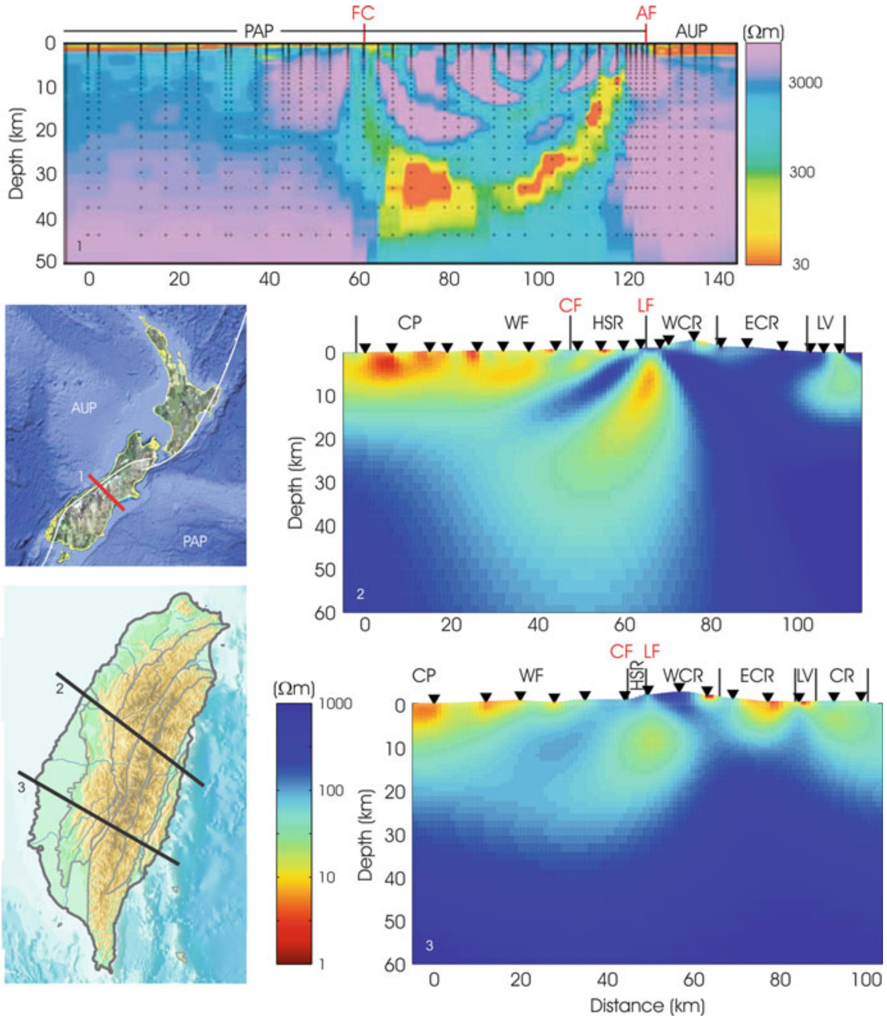

Fig. 13.27 Resistivity models of (1) New Zealand from Wannamaker et al., (2002), (2) Central Taiwan from Bertrand et al., (2009), and (3) Southern Taiwan from Bertrand (2010). In the *upper* two panels, note the zone of low resistivity extending from depths of 20–30 km to the surface, which is inferred to be a region of fluids generated by prograde metamorphism in the thickened crustal root. In Taiwan this reaches the surface at the Lishan Fault (LF) and in New Zealand this occurs beneath the Alpine Fault (AF). Note that the resistivity model of New Zealand is reversed east–west, to emphasize the similarity with Taiwan

it has a low velocity (Brown et al. 1996) and magnetotelluric data reveal a low resistivity that has been used to infer a fluid content of 5–12% (Unsworth et al. 2005) (Fig. 13.28).

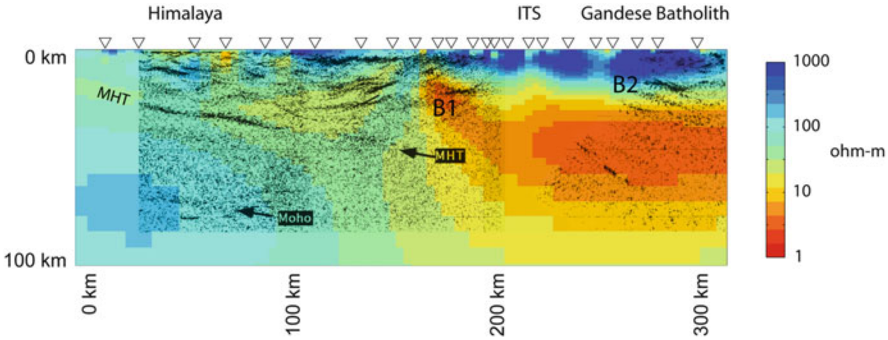

Fig. 13.28 Geophysical image of the crust below the Himalayas and southern Tibetan Plateau. *Black lines* show seismic reflection data (Nelson et al. 1996) with the Main Himalayan Thrust (MHT) interpreted as the upper surface of the underthrust Indian Plate. Triangles indicate locations where magnetotelluric (MT) data was recorded. *Colours* show electrical resistivity determined by MT exploration along the same transect (Unsworth et al. 2005). *Blues* and *green* represent the resistivity values typical of dry, cold crust and upper mantle. *Red* regions have anomalously low resistivity suggesting the presence of a fluid phase such as partial melt and/or aqueous fluids. ITS = Indus-Tsangpo suture (defines the plate boundary at the surface). B1 and B2 are seismic bright spots that are interpreted as concentrations of fluids

13.8 Conclusions

Seismic and magnetotelluric exploration are powerful tools to image fluid distribution in the crust and upper mantle. The analysis presented in this chapter shows that quantitative estimates of fluid content can be derived from both methods. As joint inversion techniques are developed to simultaneously invert both datasets, more detailed images of metasomatizing fluids will be obtained.

Acknowledgements The authors thank Michael Bostock and Nik Christensen for their reviews, and numerous colleagues for discussions on this topic over the year. We also thank the Editors for their great patience in waiting for this chapter.

References

Abers GA (2005) Seismic low-velocity layer at the top of subducting slabs beneath volcanic arcs: observations, predictions, and systematics. Phys Earth Planet Inter 149:7–29

Abers GA, MacKenzie LS, Rondenay S, Zhang Z, Wech AG, Creager KC (2009) Imaging the source region of Cascadia tremor and intermediate-depth earthquakes. Geology 37:1119–1122. doi:10.1130/G30143A.1

Aizawa Y, Barnhoorn A, Faul UH, Gerald JDF, Jackson I, Kovács I (2008) Seismic properties of Anita Bay dunite: an exploratory study of the influence of water. J Petrol 49(4):841–855. doi:10.1093/petrology/egn007

Albarède F (1998) The growth of continental crust. Tectonophysics 296:1–14

Ammon CJ, Randall GE, Zandt G (1990) On the non-uniqueness of receiver function inversions. J Geophys Res 95:15303–15319

Aprea CM, Unsworth MJ, Booker JR (1998) Resistivity structure of the Olympic mountains and Puget Lowlands. Geophys Res Lett 25:109–112

Archie GE (1942) The electrical resistivity log as an aid in determining some reservoir characteristics. Trans Am Inst Min Metall Pet Eng 146:54–62

Audet P, Bostock MG, Christensen NI, Peacock SM (2009) Seismic evidence for overpressured subducted oceanic crust and megathrust fault sealing. Nature 457:76–78. doi:10.1038/nature07650

Aulbach S, Pearson NJ, O'Reilly SY, Doyle BJ (2007) Origins of xenolithic eclogites and pyroxenites from the central Slave Craton, Canada. J Petrol 48(10):1843–1873. doi:10.1093/petrology/egm041

Austrheim H, Erambert M, Engvik AK (1997) Processing of crust in the root of the Caledonian continental collision zone: the role of eclogitization. Tectonophysics 273:129–153

Auzende AL, Pellenq RJM, Devouard B, Baronnet A, Grauby O (2006) Atomistic calculations of structural and elastic properties of serpentine minerals: the case of lizardite. Phys Chem Miner 33:266–275. doi:10.1007/s00269-006-0078-x

Babuška V, Cara M (1991) Seismic anisotropy in the earth. Kluwer, Dodrecht, 217pp

Bach W, Früh-Green G (2010) Alteration of the oceanic lithosphere and implications for seafloor processes. Elements 6:173–178

Bank CG, Bostock MG, Ellis R, Cassidy J (2000) A reconnaissance teleseismic study of the upper mantle and transition zone beneath the Archean Slave Craton in Northwest Canada. Tectonophysics 319(3):151–166

Beaumont C, Jamieson RA, Nguyen BH, Lee B (2001) Himalayan tectonics explained by extrusion of a low-viscosity crustal channel coupled to focused surface denudation. Nature 414:738–742

Bercovici D, Karato S (2003) Whole mantle convection and the transition-zone water filter. Nature 425:39–44

Berryman JG (1995) Mixture theories for rock properties. In: Ahrens TJ (ed) Rock physics and phase relations: a handbook of physics constants, vol 3, AGU reference shelf. AGU, Washington, DC, pp 205–228

Berryman JG (2007) Seismic waves in rocks with fluids and fractures. Geophys J Int 171:954–974. doi:10.1111/j.1365-246X.2007.03563.x

Bertrand EA (2010) MT study of the Taiwan arc-continent collision, Ph.D. thesis, University of Alberta, Edmonton

Bertrand EA, Unsworth MJ, Chiang CW, Chen CS, Chen CC, Wu F, Turkoglu E, Hsu HK, Hill G (2009) Magnetotelluric studies of the arc-continent collision in Central Taiwan. Geology 37:711–714

Bezacier L, Reynard B, Bass JD, Sanchez-Valle C, de Moortèle BV (2010a) Elasticity of antigorite, seismic detection of serpentinites, and anisotropy in subduction zones. Earth Planet Sci Lett 289:198–208. doi:10.1016/j/epsl.2009.11.009

Bezacier L, Reynard B, Bass JD, Wang J, Mainprice D (2010b) Elasticity of glaucophane, seismic velocities and anisotropy of the subducted oceanic crust. Tectonophysics 494:201–210. doi:10.1016/j.tecto.2010.09.011

Bina CR, Helffrich GR (1992) Calculation of elastic properties from thermodynamic equation of state principles. Annu Rev Earth Planet Sci 20:527–552

Birch F (1960) The velocity of compressional waves in rocks to 10 kilobars, Part 1. J Geophys Res 65(4):1083–1102

Blakely RJ, Brocher TM, Wells RE (2005) Subduction-zone magnetic anomalies and implications for hydrated forearc mantle. Geology 33(6):445–448

Block D (2001) Water resistivity Atlas of Western Canada Abstract, Paper presented at Rock the Foundation Convention of Canadian Society of Petroleum Geologists, Calgary, 18–22 June 2001

Booker JR, Favetto A, Pomposiello MC (2004) Low electrical resistivity associated with plunging of the Nazca flat slab beneath Argentina. Nature 429:399–403

Bostock MG (1997) Anisotropic upper-mantle stratigraphy and architecture of the Slave craton. Nature 390:392–395

Bostock MG (1998) Mantle stratigraphy and evolution of the Slave province. J Geophys Res 103 (B9):21183–21200

Bostock MG, Rondenay S (1999) Migration of scattered teleseismic body waves. Geophys J Int 137:732–746

Bostock MG, VanDecar JC (1995) Upper-mantle structure of the northern Cascadia subduction zone. Can J Earth Sci 32:1–12

Bostock MG, Hyndman RD, Rondenay S, Peacock SM (2002) An inverted continental moho and serpentinization of the forearc mantle. Nature 417:536–538

Bowring SA, Williams IS, Compston W (1989) 3.96 Ga gneisses from the Slave province, Northwest-Territories, Canada. Geology 17(11):971–975

Bowring SA, Housh TB, Isachsen CE (1990) The Acasta gneisses: remnant of Earth's early crust. In: Newsom HE, Jones JH (eds) Origin of the Earth. Oxford University Press, Oxford, UK, pp 319–343

Brasse H, Kapinos Li Y, Mutschard SW, Eydam D (2009) Structural electrical aniostropy in the crust at the south-Central Chilean continental margin as inferred from geomagnetic transfer functions. Phys Earth Planet Inter 173:7–16

Brenan JM, Watson EB (1988) Fluids in the lithosphere, 2. Experimental constraints on CO2 transport in dunite and quartzite at elevated P-T conditions with implications for mantle and crustal decarbonation processes. Earth Planet Sci Lett 91:141–158

Brenders AJ, Pratt RG (2007) Full waveform tomography for lithospheric imaging: results from a blind test in a realistic crustal model. Geophys J Int 168:133–151. doi:10.1111/j.1365-246X.2006.03,156.x

Brocher T, Parsons T, Trehu AM, Snelson CM, Fisher MA (2003) Seismic evidence for widespread serpentinized forearc upper mantle along the Cascadia margin. Geology 31(3):267–270

Brown LD, Zhao W, Nelson KD, Hauck M, Alsdorf D, Ross A, Cogan M, Clark M, Liu X, Che J (1996) Bright spots, structure and magmatism in southern Tibet from INDEPTH seismic reflection profiling. Science 274:1688–1690

Brown JR, Beroza GC, Ide S, Ohta K, Shelly DR, Schwartz SY, Rabbel W, Thorwart M, Kao H (2009) Deep low-frequency earthquakes in tremor localize to the plate interface in multiple subduction zones. Geophys Res Lett 36:L19306. doi:10.1029/2009GL040027

Brudzinski MR, Thurber CH, Hacker BR, Engdahl ER (2007) Global prevalence of double Benioff zones. Science 316:1472–1474. doi:10.1126/science.1139204

Calvert AJ (1996) Seismic reflection constraints on imbrication and underplating of the northern Cascadia convergent margin. Can J Earth Sci 33:1294–1307

Calvert AJ (2004) Seismic reflection imaging of two megathrust shear zones in the northern Cascadia subduction zone. Nature 428:163–167. doi:10.1038/nature02372

Calvert AJ, Clowes RM (1990) Deep, high-amplitude reflections from a major shear zone above the subducting Juan de Fuca plate. Geology 18:1091–1094

Calvert AJ, Sawyer EW, Davis WJ, Ludden JN (1995) Archaean subduction inferred from seismic images of a mantle suture in the Superior Province. Nature 375:670–673

Cammarano F, Romanowicz B (2008) Radial profiles of seismic attenuation in the upper mantle based on physical models. Geophys J Int 175:116–134. doi:10.1111/j.1365-246X.2008.03863.x

Cassidy JF, Bostock MG (1996) Shear-wave splitting above the subducting Juan de Fuca plate. Geophys Res Lett 23:941–944

Chen CW, Rondenay S, Weeraratne D, Snyder DB (2007) New constraints on the upper mantle structure of the slave craton from rayleigh wave inversion. Geophys Res Lett 34:L10301. doi:10.1029/2007GL029535

Chen CW, Rondenay S, Evans RL, Snyder DB (2009) Geophysical detection of relict metasomatism from an Archean (ca 3.5 Ga) subduction zone. Science 326:1089–1091. doi:10.1126/science.1178477

Christensen NI (1966) Elasticity of ultrabasic rocks. J Geophys Res 71(24):5921–5931

Christensen NI (1984) Pore pressure and oceanic crustal seismic structure. Geophys J R Astr Soc 79:411–423

Christensen NI (1989) Reflective and seismic properties of the deep continental crust. J Geophys Res 94:17793–17804

Christensen NI (1996) Poisson's ratio and crustal seismology. J Geophys Res 101:3139–3156

Christensen NI (2004) Serpentinites, peridotites, and seismology. Int Geol Rev 46:795–816

Clowes RM, Brandon MT, Green AG, Yorath CJ, Sutherland Brown A, Kanasewich ER, Spencer C (1987) Lithoprobe-southern Vancouver Island: cenozoic subduction complex imaged by deep seismic reflections. Can J Earth Sci 24:31–51

Crampin S, Booth DC (1985) Shear-wave polarizations near the North Anatolian Fault – II. Interpretation in terms of crack-induced anisotropy. Geophys J R Astr Soc 83:75–92

Currie CA, Cassidy JF, Hyndman RD, Bostock MG (2004) Shear wave anisotropy beneath the Cascadia subduction zone and western North American craton. Geophys J Int 157:341–353. doi:10.1111/j.1365-246X.2004.02175.x

de Wit M, Roehring C, Hart RJ, Armstrong RA, de Ronde CEJ, Green RWE, Tredoux M, Peberdy E, Hart RA (1992) Formation of an Archaean continent. Nature 357:553–562

DeMets C, Gordon RG, Argus DF, Stein S (1994) Effect of recent revisions to the geomagnetic reversal time-scale on estimates of current plate motions. Geophys Res Lett 21(20):2191–2194

Dueker KG, Sheehan AF (1997) Mantle discontinuity structure from midpoint stacks of converted p to s waves across the Yellowstone hotspot track. J Geophys Res 102:8313–8327

Dunn RA, Toomey DR (2001) Crack-induced seismic anisotropy in the oceanic crust across the East Pacific rise (9°30′N). Earth Planet Sci Lett 189:9–17

Dziewonski AM, Anderson DL (1981) Preliminary reference earth model. Phys Earth Planet Inter 25:297–356

Eisel M, Haak V (1999) Macro-anisotropy of the electrical conductivity of the crust: a magnetotelluric study of the German continental deep drilling site (KTB). Geophys J Int 136:109–122

Ellis DV, Singer JM (2008) Well logging for Earth scientists, 2nd edn. Springer, Berlin. ISBN 978-1-4020-3738-2

Evans RL, Chave AD, Booker JR (2002) On the importance of offshore data for magnetotelluric studies of ocean-continent subduction systems. Geophys Res Lett 29(9):1302. doi:10.1029/2001GL013960

Faul UH, Gerald JDF, Jackson I (2004) Shear wave attenuation and dispersion in melt-bearing olivine polycrystals: 2. Microstructural interpretation and seismological implications. J Geophys Res 109:B06202. doi:10.1029/2003JB002407

Flueh ER, Fisher MA, Bialas J, Childs JR, Klaeschen D, Kukowski N, Parsons T, Scholl DW, ten Brink U, Tréhu AM, Vidal N (1998) New seismic images of the Cascadia subduction zone from cruise SO108 – ORWELL. Tectonophysics 293:69–84

Fouch MJ, Rondenay S (2006) Seismic anisotropy beneath stable continental interiors. Phys Earth Planet In 158:292–320

Frisillo AL, Barsch GR (1972) Measurement of single-crystal elastic constants of bronzite as a function of pressure and temperature. J Geophys Res 77(32):6360–6384

Gaillard F (2004) Laboratory measurements of electrical conductivity of hydrous and dry silicic melts under pressure. Earth Planet Sci Lett 218:215–228

Gao S, Rudnick RL, Carlson RW, McDonough WF, Liu YS (2002) Re-Os evidence for replacement of ancient mantle lithosphere beneath the North China craton. Earth Planet Sci Lett 198:307–322

Gatzemeier A, Moorkamp M (2004) 3D modelling of electrical anisotropy from electromagnetic array data: hypothesis testing for different upper mantle conduction mechanisms. Phys Earth Planet Inter 149:225–242

Gibert F, Guillaume D, Laporte D (1998) Importance of fluid immiscibility in the H2O- NaCl-CO2 system and selective CO2 entrapment in granulites: experimental phase diagram at 5–7 kbar, 900°C and wetting textures. Eur J Mineral 10:1109–1123

Glover P, Hole MJ, Pous J (2000) A modified Archie's Law for two conducting phases. Earth Planet Sci Lett 180:369–383

Green HW, Houston H (1995) The mechanics of deep earthquakes. Annu Rev Earth Planet Sci 23:169–213

Green AG, Clowes RM, Yorath CJ, Spencer C, Kanasewich ER, Brandon MT, Sutherland Brown A (1986) Seismic reflection imaging of the subducting Juan de Fuca plate. Nature 319:210–213

Gribb TT, Cooper RF (2000) The effect of an equilibrated melt phase on the shear creep and attenuation behavior of polycrystalline olivine. Geophys Res Lett 27(15):2341–2344

Grove TL, Chatterjee N, Parman SW, Médard E (2006) The influence of H2O on mantle wedge melting. Earth Planet Sci Lett 249:74–89

Hacker BR (2008) H_2O subduction beneath arcs. Geochem Geophys Geosyst 9. doi:10.1029/2007GC001707

Hacker BR, Abers GA (2004) Subduction factory 3. An excel worksheet and macro for calculating the densities, seismic wave speeds, and H2O contents of minerals and rocks at pressure and temperature. Geochem Geophys Geosyst 5:Q01005. doi:10.1029/2003GC000614

Hacker B, Abers G, Peacock S (2003a) Subduction factory 1: theoretical mineralogy, density, seismic wave-speeds, and H2O content. J Geophys Res 108(B1):2029. doi:10.1029/2001JB001127

Hacker BR, Peacock SM, Abers GA, Holloway SD (2003b) Subduction factory 2. Are intermediate-depth earthquakes in subducting slabs linked to metamorphic dehydration reactions? J Geophys Res 108(B1):2030. doi:10.1029/2001JB001129

Hammond WC, Humphreys ED (2000a) Upper mantle seismic wave attenuation: effects of realistic partial melt distribution. J Geophys Res 105:10987–10999

Hammond WC, Humphreys ED (2000b) Upper mantle seismic wave velocity: effects of realistic partial melt geometries. J Geophys Res 105:10975–10986

Hasalová P, Schulmann K, Lexa O, Štípská P, Hrouda F, Ulrich S, Haloda J, Týcová P (2008) Origin of migmatites by deformation-enhanced melt infiltration of orthogneiss: a new model based on quantitative microstructural analysis. J Metamorph Geol 26:29–53

Heaman LM, Kjarsgaard RA, Creaser RA, Cookenboo HO, Kretschmar U (1997) Multiple episodes of kimberlite magmatism in the Slave province, North America. In: Lithoprobe report vol 56, Lithoprobe Secretariat, Vancouver, pp 14–17

Heise W, Pous J (2003) Anomalous phases exceeding 90^{o} in magnetotellurics: anisotropic model studies and a field example. Geophys J Int 155:308–318

Helffrich GR (1996) Subducted lithospheric slab velocity structure: observations and mineralogical inferences. In: Bebout G, Scholl D, Kirby S, Platt J (eds) Subduction top to bottom, vol 96, AGU geophysical monograph. AGU, Washington, DC, pp 215–222

Helmstaedt H, Schulze DJ (1989) Southern African kimberlites and their mantle sample: implications for Archean tectonic and lithosphere evolution. In: Ross J (ed) Kimberlites and related rocks, vol 1, Their composition, occurrence, origin, and emplacement. Blackwell, Carlton, pp 358–368

Hilairet N, Daniel I, Reynard B (2006) Equation of state of antigorite, stability field of serpentines, and seismicity in subduction zones. Geophys Res Lett 33:L02302. doi:10.1029/2005GL024728

Holness MB (1992) Equilibrium dihedral angles in the system quartz-CO2–H2O-NaCl at 800°C and 1–15 kbar: the effects of pressure and fluid composition on the permeability of quartzites. Earth Planet Sci Lett 114:171–184

Holness MB (1993) Temperature and pressure dependence of quartz-aqueous fluid dihedral angles: the control of adsorbed H_2O on the permeability of quartzites. Earth Planet Sci Lett 117:363–377

Holness MB (2006) Melt-solid dihedral angles of common minerals in natural rocks. J Petrol 47(4):791–800

Hyndman RD (1988) Dipping seismic reflectors, electrically conductive zones, and trapped water in the crust over a subducting plate. J Geophys Res 93:13391–13405

Hyndman RD, Klemperer SL (1989) Lower-crustal porosity from electrical measurements and inferences about composition from seismic velocities. Geophys Res Lett 16(3):255–258

Hyndman RD, Peacock SM (2003) Serpentinization of the forearc mantle. Earth Planet Sci Lett 212:417–432

Hyndman RD, Shearer PM (1989) Water in the lower continental crust: modelling magnetotelluric and seismic reflection results. Geophys J Int 98:343–365

Hyndman RD, Wang K (1993) Thermal constraints on the zone of major thrust earthquake failure: the Cascadia subduction zone. J Geophys Res 98:2039–2060

Ito K (1990) Effects of H_2O on elastic velocities in ultrabasic rocks at 900°C under 1 GPa. Phys Earth Planet Inter 61:260–268

Jackson I, Paterson MS, Gerald JDF (1992) Seismic wave dispersion and attenuation in Åheim dunite: an experimental study. Geophys J Int 108:517–534

Jackson JA, Austrheim H, McKenzie D, Priestley K (2004) Metastability, mechanical strength, and the support of mountain belts. Geology 32(7):625–628

Jodicke H, Jording A, Ferrari L, Arzate J, Mezger K, Rupke L (2006) Fluid release from the subducted Cocos Plate and partial melting of the crust deduced from magnetotelluric studies in Southern Mexico: implications for the generation of volcanism and subduction dynamics. J Geophys Res 111:B08102. doi:10.1029/2005JB003739

Jones AG, Ferguson IJ (2001) The electric Moho. Nature 409:331–333

Jones AG, Ferguson IJ, Chave AD, Evans RL, McNeice GW (2001) Electric lithosphere of the Slave craton. Geology 29(5):423–426

Jordan TH (1978) Composition and development of the continental tectosphere. Nature 274:544–548

Jung H, Karato S (2001) Water-induced fabric transitions in olivine. Science 293:1460–1463

Kamiya S, Kobayashi Y (2000) Seismological evidence for the existence of serpentinized wedge mantle. Geophys Res Lett 27(6):819–822

Karato S (1990) The role of hydrogen in the electrical conductivity of the upper mantle. Nature 347:272–273

Karato S (1995) Effects of water on seismic wave velocities in the upper mantle. Proc Jpn Acad 71:61–66

Karato S (2003) Mapping water content in the upper mantle. In: Eiler JM (ed) Inside the subduction factory, vol 138, AGU geophysical monograph. AGU, Washington, DC, pp 135–152

Karato S (2006) Remote sensing of hydrogen in Earth's mantle. Rev Mineral Geochem 62:343–375. doi:10.2138/rmg.2006.62.15

Karato S, Jung H (1998) Water, partial melting and the origin of the seismic low velocity and high attenuation zone in the upper mantle. Earth Planet Sci Lett 157:193–207

Karato S, Jung H (2003) Effects of pressure on high-temperature dislocation creep in olivine. Philos Mag 83(3):401–414. doi:10.1080/0141861021000025829

Katayama I, Hirauchi K, Michibayashi K, Ando J (2009) Trench-parallel anisotropy produced by serpentine deformation in the hydrated mantle wedge. Nature 461:1114–1117. doi:10.1038/nature08513

Kellett RL, Mareschal M, Kurtz RD (1992) A model of lower crustal electrical anisotropy for the Pontiac Subprovince of the Canadian shield. Geophys J Int 111:141–150

Kern H, Liu B, Popp T (1997) Relation between anisotropy of P and S wave velocities and anisotropy of attenuation in serpentinite and amphibolite. J Geophys Res 102:3051–3065

Kirby S, Engdahl ER, Denlinger R (1996) Intermediate-depth intraslab earthquakes and arc volcanism as physical expressions of crustal and uppermost mantle metamorphism in subducting slabs. In: Bebout G, Scholl D, Kirby S, Platt J (eds) Subduction top to bottom, vol 96, AGU geophysical monograph. AGU, Washington, DC, pp 195–214

Kono Y, Ishikawa M, Arima M (2007) Effect of H2O released by dehydration of serpentine and chlorite on compressional wave velocities of peridotites at 1 GPa and up to 1000°C. Phys Earth Planet Inter 161:215–223. doi:10.1016/j.pepi.2007.02.005

Kumazawa M, Anderson OL (1969) Elastic moduli, pressure derivatives, and temperature derivatives of single-crystal olivine and single-crystal forsterite. J Geophys Res 74 (25):5961–5972

Kurtz RD, Delaurier JM, Gupta JC (1986) A magnetotelluric sounding across Vancouver Island detects the subducting Juan-de-Fuca plate. Nature 321:596–599

Kurtz RD, Delaurier JM, Gupta JC (1990) The electrical-conductivity distribution beneath Vancouver Island – a region of active plate subduction. J Geophys Res 95:10929–10946

Langston CA (1977) Corvallis, Oregon, crustal and upper mantle receiver structure from teleseismic p and s waves. Bull Seismol Soc Am 67(3):713–724

Langston CA (1979) Structure under Mount Rainier, Washington, inferred from teleseismic body waves. J Geophys Res 84:4749–4762

Leaver DS, Mooney WD, Kohler WM (1984) A seismic refraction study of the Oregon Cascades. J Geophys Res 89:3121–3134

Lee CTA (2003) Compositional variations of density and seismic velocities in natural peridotites at STP conditions: implications for seismic imaging of compositional heterogeneities in the upper mantle. J Geophys Res 108:2441. doi:10.1029/2003JB002413

Lenardic A, Moresi L, Mühlhaus H (2000) The role of mobile belts for the longevity of deep cratonic lithosphere: the crumple zone model. Geophys Res Lett 27(8):1235–1238

Lenardic A, Moresi LN, Mühlhaus H (2003) Longevity and stabilty of cratonic lithosphere: insights from numerical simulations of coupled mantle convection and continental tectonics. J Geophys Res 108(B6):2303. doi:10.1029/2002JB001859

Levander A, Niu F, Lee CTA, Cheng X (2006) Imag(in)ing the continental lithosphere. Tectonophysics 416:167–185. doi:10.1016/j/tecto.2005.11.018

Lewis C, Ray D, Chiu KK (2007) Primary geologic sources of arsenic in the Chianan plain (blackfoot disease area) and the Lanyang plain of Taiwan. Int Geol Rev 49:947–961

Li S, Unsworth MJ, Booker JR, Wei W, Tan H, Jones AG (2003) Partial melt or aqueous fluid in the mid-crust of Southern Tibet? Constraints from INDEPTH magnetotelluric data. Geophys J Int 153:289–304

Long MD, Silver PG (2008) The subduction zone flow field from seismic anisotropy: a global view. Science 319:315–318. doi:10.1126/science.1150809

Ludden J, Hubert C (1986) Geologic evolution of the late Archean Abitibi greenstone belt of Canada. Geology 14:707–711

Mainprice D, Ildefonse B (2009) Seismic anisotropy of subduction zone minerals – contribution of hydrous phases. In: Lallemand S, Funiciello F (eds) Subduction zone geodynamics. Springer, Berlin/Heidelberg, pp 63–84

Mainprice D, Le Page Y, Rodgers J, Jouanna P (2008) Ab initio elastic properties of talc from 0 to 12 GPa: interpretation of seismic velocities at mantle pressures and prediction of auxetic behaviour at low pressure. Earth Planet Sci Lett 274:327–338. doi:10.1016/j.epsl.2008.07.047

Mamaus J, Laporte D, Schiano P (2004) Dihedral angle measurements and infiltration property of SiO2 rich melts in mantle peridotite assemblages. Contrib Mineral Petrol 148:1–12

Mareschal M, Kellett RL, Kurtz RD, Ludden JN, Ji S, Bailey RC (1995) Archaean cratonic roots, mantle shear zones and deep electrical anisotropy. Nature 375:134–137

Matthews DH (1986) Seismic reflections from the lower crust around Britain. In: Dawson JB, Carswell DA, Hall J, Wedepohl KH (eds) The nature of the lower continental crust, vol 24, Special publication. Geological Society, London, pp 11–24

Meju MA (2000) Geoelectric investigation of old/abandoned, covered landfill sites in urban areas: model development with a genetic diagnosis approach. J Appl Geophys 44:115–150

Mercier JP, Bostock MG, Audet P, Gaherty JB, Garnero EJ, Revenaugh J (2008) The teleseismic signature of fossil subduction: Northwestern Canada. J Geophys Res 113:B04308. doi:10.1029/2007JB005127

Miller KC, Keller GR, Gridley JM, Luetgert JH, Mooney WD, Thybo H (1997) Crustal structure along the west flank of the Cascades, western Washington. J Geophys Res 102:17857–17873

Minster JB, Anderson DL (1981) A model of dislocation-controlled rheology for the mantle. Philos Trans R Soc Lond A 299:319–356

Moorkamp M, Jones AG, Eaton DW (2007) Joint inversion of teleseismic receiver functions and magnetotelluric data using a genetic algorithm: are seismic velocities and electrical conductivities compatible? Geophys Res Lett 34:L16311. doi:10.1029/2007GL030519

Moorkamp M, Jones AG, Fishwick S (2010) Joint inversion of receiver functions, surface wave dispersion, and magnetotelluric data. J Geophys Res 115:B04318. doi:10.1029/2009JB006369

Murphy WF (1985) Sonic and ultrasonic velocities: theory versus experiment. Geophys Res Lett 12(2):85–88

Nelson KD, Zhao W, Brown LD, Kuo J, Che J, Liu X, Klemperer SL, Makovsky Y, Meissner R, Mechie J, Kind R, Wenzel F, Ni J, Nablek J, Leshou C, Tan H, Wei W, Jones AG, Booker JR, Unsworth MJ, Kidd WSF, Hauck M, Alsdorf D, Ross A, Cogan M, Wu C, Sandvol E, Edwards M (1996) Partially molten Middle Crust Beneath Southern Tibet: synthesis of project INDEPTH results. Science 274:1684–1686

Nesbitt B (1993) Electrical resistivities of crustal fluids. J Geophys Res 98:4301–4310

Nicholson T, Bostock M, Cassidy J (2005) New constraints on subduction zone structure in northern Cascadia. Geophys J Int 161(3):849–859

Nolet G (2008) A breviary of seismic tomography. Cambridge University Press, Cambridge, UK

O'Connell RJ, Budiansky B (1974) Seismic velocities in dry and saturated cracked solids. J Geophys Res 79(35):5412–5426

O'Connell RJ, Budiansky B (1977) Viscoelastic properties of fluid-saturated cracked solids. J Geophys Res 82(36):5719–5735

O'Neill C, Jellinek AM, Lenardic A (2007) Conditions for the onset of plate tectonics on terrestrial planets and moons. Earth Planet Sci Lett 261:20–32

Obara K (2002) Nonvolcanic deep tremor associated with subduction in Southwest Japan. Science 296:1679–1681

Obara K, Hirose H, Yamamizu F, Kasahara K (2004) Episodic slow slip events accompanied by non-volcanic tremors in southwest Japan subduction zone. Geophys Res Lett 23:L23602. doi:10.1029/2004GL020848

Park J, Yuan H, Levin V (2004) Subduction zone anisotropy beneath Corvallis, Oregon: a serpentinite skid mark of trench-parallel terrane migration? J Geophys Res 109:B10306. doi:10.1029/2003JB002718

Parsons T, Blakely RJ, Brocher TM, Christensen NI et al (2005) Crustal structure of the Cascadia fore arc of Washington. USGS professional paper 1661-D, USGS, Denver, 45 pp

Partzsch GM, Schilling FR, Arndt J (2000) The influence of partial melting on the electrical behavior of crustal rocks: laboratory examinations, model calculations and geological interpretations. Tectonophysics 317:189–203

Payero JS, Kostoglodov V, Shapiro N, Mikumo T, Iglesias A, Perez-Campos X, Clayton RW (2008) Nonvolcanic tremor observed in the Mexican subduction zone. Geophys Res Lett 35: L07305. doi:10.1029/2007GL032877

Peterson CL, Christensen DH (2009) Possible relationship between nonvolcanic tremor and the 1998–2001 slow slip event, south central Alaska. J Geophys Res 114:B06302. doi:10.1029/2008JB006096

Pozgay SH, Wiens DA, Conder JA, Shiobara H, Sugioka H (2009) Seismic attenuation tomography of the Mariana subduction system: implications for thermal structure, volatile distribution, and slow spreading dynamics. Geochem Geophys Geosyst 10(4):Q04X05. doi:10.1029/2008GC002313

Preston LA, Creager KC, Crosson RS, Brocher TM, Tréhu AM (2003) Intraslab earthquakes: dehydration of the Cascadia slab. Science 302:1197–1200

Prouteau G, Scaillet B, Pichavant M, Maury R (2001) Evidence for mantle metasomatism by hydrous silicic melts derived from subducted oceanic crust. Nature 410:197–200

Quist AS, Marshall WL (1968) Electrical conductances of aqueous sodium chloride solutions from 0–800°C and at pressures to 4000 Bars. J Phys Chem 72:684–703

Ramachandran K, Hyndman RD, Brocher TM (2006) Regional P wave velocity structure of the Northern Cascadia subduction zone. J Geophys Res 111:B12301. doi:10.1029/2005JB004108

Ranero CR, Morgan JP, McIntosh K, Reichert C (2003) Bending-related faulting and mantle serpentenization at the Middle America trench. Nature 425:367–373

Rasmussen J, Humphreys E (1988) Tomographic image of the Juan de Fuca plate beneath Washington and western Oregon using teleseismic P-wave travel times. Geophys Res Lett 15:1417–1420

Reynard B, Hilairet N, Balan E, Lazzeri M (2007) Elasticity of serpentines and extensive serpentinization in subduction zones. Geophys Res Lett 34:L13307. doi:10.1029/2007GL030176

Roberts JJ, Tyburczy JA (1999) Partial-melt electrical conductivity: influence of melt composition. J Geophys Res 104:7055–7065

Rodi W, Mackie RL (2001) Nonlinear conjugate gradients algorithm for 2-D magnetotelluric inversion. Geophysics 66:174–187

Rogers G, Dragert H (2003) Episodic tremor and slip on the Cascadia subduction zone: the chatter of silent slip. Science 300:1942–1943

Romanyuk TV, Blakely R, Mooney WD (1998) The Cascadia subduction zone: two contrasting models of lithospheric structure. Phys Chem Earth 23(3):297–301

Rondenay S (2009) Upper mantle imaging with array recordings of converted and scattered teleseismic waves. Surv Geophys 30:377–405. doi:10.1007/s10712-009-9071-5

Rondenay S, Bostock MG, Hearn TM, White DJ, Ellis RM (2000) Lithospheric assembly and modification of the SE Canadian Shield: Abitibi-Grenville teleseismic experiment. J Geophys Res 105(B6):13735–13754

Rondenay S, Bostock MG, Shragge J (2000) Multiparameter two-dimensional inversion of scattered teleseismic body waves, 3, application to the Cascadia 1993 data set. J Geophys Res 106:30795–30808

Rondenay S, Abers GA, van Keken PE (2008) Seismic imaging of subduction zone metamorphism. Geology 36:275–278

Roth JB, Fouch MJ, James DE, Carlson RW (2008) Three-dimensional seismic velocity structure of the northwestern United States. Geophys Res Lett 35:L15304. doi:10.1029/2008GL034669

Rüpke LH, Morgan JP, Hort M, Connolly JA (2004) Serpentine and the subduction zone water cycle. Earth Planet Sci Lett 223:17–34

Rychert CA, Rondenay S, Fischer KM (2007) P-to-S and S-to-P imaging of a sharp lithosphere-asthenosphere boundary beneath eastern North America. J Geophys Res 112(B8):B08314. doi:10.1029/2007GL029535

Savage MK (1999) Seismic anisotropy and mantle deformation: what have we learned from shear wave splitting? Rev Geophys 37(1):65–106

Schilling FR, Sinogeikin SV, Bass JD (2003) Single-crystal elastic properties of lawsonite and their variation with temperature. Phys Earth Planet Inter 136:107–118. doi:10.1016/S0031-9201(03), 00024-4

Schmeling H (1985) Numerical models on the influence of partial melt on elastic, anelastic and electric properties of rocks. Part I: elasticity and anelasticity. Phys Earth Planet Inter 41:34–57

Schulmann K, Martelat JE, Ulrich S, Lexa O, Štípská P, Becker JK (2008) Evolution of microstructure and melt topology in partially molten granitic mylonite: implications for rheology of felsic middle crust. J Geophys Res 113:B10406

Shapiro NM, Campillo M, Stehly L, Ritzwoller MH (2005) High-resolution surface-wave tomography from ambient seismic noise. Science 307:1615–1618. doi:10.1126/science.1108339

Shelly DR, Beroza GC, Ide S, Nakamula S (2006) Low-frequency earthquakes in Shikoku, Japan, and their relationship to episodic tremor and slip. Nature 442:188–191. doi:10.1038/nature04931

Silver PG (1996) Seismic anisotropy beneath the continents: probing the depths of geology. Annu Rev Earth Planet Sci 24:385–432

Simpson F (2001) Resistance to mantle flow inferred from the electromagnetic strike of the Australian upper mantle. Nature 412:632–635

Simpson F, Bahr K (2005) Practical magnetotellurics. Cambridge University Press, Cambridge, UK

Simpson F, Tommasi A (2005) Hydrogen diffusivity and electrical anisotropy of a peridotite mantle. Geophys J Int 160:1092–1102

Siripunvaraporn W, Egbert GD, Lenbury Y, Uyeshima M (2005) Three dimensional magnetotelluric inversion: data subspace method. Phys Earth Planet Inter 150:3–14

Snyder DB, Bostock MG, Lockhart GD (2003) Two anisotropic layers in the Slave craton. Lithos 71:529–539

Snyder DB, Rondenay S, Bostock MG, Lockhart GD (2004) Mapping the mantle lithosphere for diamond potential. Lithos 77:859–872

Soyer W, Unsworth M (2006) Deep electrical structure of the northern Cascadia (British Columbia, Canada) subduction zone: implications for the distribution of fluids. Geology 34(1):53–56. doi:10.1130/G21951.1

Stachnik J, Abers G, Christensen D (2004) Seismic attenuation and mantle wedge temperatures in the Alaska subduction zone. J Geophys Res 109:B10304. doi:10.1029/2004JB003018

Stetsky RM, Brace WF (1973) Electrical conductivity of serpentinized rocks to 6 kilobars. J Geophys Res 78:7614–7621

Strack KM, Luschen E, Kotz AW (1990) Long-offset transient electromagnetic (LOTEM) depth soundings applied to crustal studies in the Black Forest and Swabian Alb, Federal Republic of Germany. Geophysics 55:834–842

Suetnova EI, Carbonell R, Smithson SB (1994) Bright seismic reflections and fluid movement by porous flow in the lower crust. Earth Planet Sci Lett 126:161–169

Takei Y (2002) Effect of pore geometry on V_P/V_S: from equilibrium geometry to crack. J Geophys Res 107:2043. doi:10.1029/2001JB000522

Takei Y, Holtzman BK (2009a) Viscous constitutive relations of solid-liquid composites in terms of grain boundary contiguity: 1. Grain boundary diffusion control models. J Geophys Res 114: B06205. doi:10.1029/2008JB005850

Takei Y, Holtzman BK (2009b) Viscous constitutive relations of solid-liquid composites in terms of grain boundary contiguity: 2. Compositional model for small melt fractions. J Geophys Res 114:B06206. doi:10.1029/2008JB005851

Takei Y, Holtzman BK (2009c) Viscous constitutive relations of solid-liquid composites in terms of grain boundary contiguity: 3. Causes and consequences of viscous anisotropy. J Geophys Res 114:B06207. doi:10.1029/2008JB005852

Tape C, Liu Q, Maggi A, Tromp J (2010) Seismic tomography of the southern California crust based on spectral-element and adjoint methods. Geophys J Int 180:433–462. doi:10.1111/j.1365-246X.2009.04429.x

ten Grotenhuis SM, Drury MR, Peach CJ, Spiers CJ (2004) Electrical properties of fine-grained olivine: evidence for grain boundary transport. J Geophys Res 109:B06203. doi:10.1029/2003JB002799

ten Grotenhuis SM, Drury MR, Spiers CJ, Peach CJ (2005) Melt distribution in olivine rocks based on electrical conductivity measurements. J Geophys Res 110:B12201. doi:10.1029/2004JB003462

Tréhu AM, Asudeh I, Brocher TM, Luetgert JH, Mooney WD, Nabelek JL, Nakamura Y (1994) Crustal architecture of the Cascadia forearc. Science 266:237–243

Tullis J, Yund R, Farver J (1996) Deformation enhanced fluid distribution in feldspar aggregates and implications for ductile shear zones. Geology 24:63–66

Ucok H, Ershaghi I, Olhoeft G (1980) Electrical resistivity of geothermal brines. J Petrol Technol 32:717–727, June 1980

Unsworth MJ (2010) Geophysics 424 class notes at University of Alberta. http://www.ualberta.ca/~unsworth/UA-classes/424/424index.html

Unsworth MJ, Jones AG, Wei W, Marquis G, Gokarn S, Spratt J (2005) Crustal rheology of the Himalaya and Southern Tibet inferred from magnetotelluric data. Nature 438:78–81. doi:10.1038/nature04154

Ussher G, Harvey C, Johnstone R, Anderson E (2000) Understanding the resistivities observed in Geothermal systems. In: Proceedings World Geothermal Congress, Kyushu

VanDecar JC (1991) Upper-mantle structure of the Cascadia subduction zone from non-linear teleseismic travel-time inversion. Ph.D. thesis, University of Washington, Seattle

Vanyan L (2002) A geoelectric model of the Cascadia Subduction zone. Izv Phys Solid Earth 38:816–845

Vinnik L (1977) Detection of waves converted from P to SV in the mantle. Phys Earth Planet Inter 15:39–45

Vry J, Powell R, Golden KM, Petersen K (2010) The role of exhumation in metamorphic dehydration and fluid production. Nat Geosci 3:31–35

Wannamaker PE (1986) Electrical conductivity of water- undersaturated crustal melting. J Geophys Res 91:6321–6327

Wannamaker PE (2000) Comment on “The petrologic case for a dry lower crust” by BWD Yardley and JW Valley. J Geophys Res 105(B3):6057–6064

Wannamaker PE (2005) Anisotropy versus heterogeneity in continental solid earth electromagnetic studies: fundamental response characteristics and implications for physiochemical state. Surv Geophys 26:733–765

Wannamaker PE (2010) Water from stone. Nat Geosci 3:10–11

Wannamaker PE, Booker JR, Jones AG, Chave AD, Filloux JH, Waff HS, Law LK (1989) Resistivity cross section through the Juan de Fuca subduction system and its tectonic implications. J Geophys Res 94:14127–14144

Wannamaker PE, Jiracek GR, Stodt JA, Caldwell TG, Gonzalez V, McKnight J, Porter AD (2002) Fluid generation and pathways beneath an active compressional orogen, the New Zealand Southern Alps, inferred from magnetotelluric data. J Geophys Res 107. doi:2001JB000186

Wannamaker PE, Caldwell TG, Jiracek GR, Maris V, Hill GJ, Ogawa Y, Bibby HM, Bennie SL, Heise W (2009) Fluid and deformation regime at an advancing subduction system at Marlborough, New Zealand. Nature 460:733–737

Watson E, Brenan JM (1987) Fluids in the lithosphere, 1. Experimentally determined wetting characteristics of CO2-H2O fluids and their implications for fluid transport, host-rock physical properties and fluid inclusion formation. Earth Planet Sci Lett 85:497–515

Wells RE, Blakely RJ, Weaver CS (2002) Cascadia microplate models and within-slab earthquakes. In: Kirby S,Wang K, Dunlop S (eds) The Cascadia subduction zone and related subduction systems – Seismic structure, intraslab earthquakes and processes, and earthquake hazards, Open-File Report, vol 02–328, US Geological Survey, Menlo Park, pp 17–23

Wiens DA, Conder JA, Faul UH (2008) The seismic structure and dynamics of the mantle wedge. Annu Rev Earth Planet Sci 36:421–455

Williams Q, Hemley RJ (2001) Hydrogen in the deep earth. Annu Rev Earth Planet Sci 29:365–418

Wilson DS (2002) The Juan de Fuca plate and slab: Isochron structure and Cenozoic plate motions. In: Kirby S, Wang K, Dunlop S (eds) The Cascadia subduction zone and related subduction systems – Seismic structure, intraslab earthquakes and processes, and earthquake hazards, Open-File Report, vol 02–328, US Geological Survey, Menlo Park, pp 9–12

Winkler KW, Murphy WF (1995) Acoustic velocity and attenuation in porous rocks. In: Ahrens TJ (ed) Rock physics and phase relations: a handbook of physics constants, vol 3, AGU reference shelf. AGU, Washington, DC, pp 20–34

Worthington PF (1993) The uses and abuses of the Archie equations, 1: the formation factor-porosity relationship. J Appl Geophys 30:215–228

Worzewski T, Jegen M, Kopp H, Brasse H, Castillo WT, Magnetotelluric image of the fluid cycle in the Costa Rican subduction zone, Nature Geoscience, 4, 108–111, 2010.

Xue M, Allen RM (2007) The fate of the Juan de Fuca plate: implications for a Yellowstone plume head. Earth Planet Sci Lett 264:266–276. doi:10.1016/j.epsl.2007.09.047

Yardley B, Valley J (1997) The petrologic case for a dry lower crust. J Geophys Res 102:12173–12185

Zhao D, Wang K, Rogers GC, Peacock SM (2001) Tomographic image of low P velocity anomalies above slab in northern Cascadia subduction zone. Earth Planet Space 53:285–293

Zhu L, Kanamori H (2000) Moho depth variation in southern California from teleseismic receiver functions. J Geophys Res 105:2969–2980